



# 1 Prior biosphere model impact on global terrestrial CO<sub>2</sub> fluxes estimated 2 from OCO-2 retrievals

3 Sajeev Philip<sup>1,2</sup>, Matthew S. Johnson<sup>1</sup>, Christopher Potter<sup>1</sup>, Vanessa Genovesse<sup>3,1</sup>, David F. Baker<sup>4,5</sup>,  
4 Katherine D. Haynes<sup>6</sup>, Daven K. Henze<sup>7</sup>, Junjie Liu<sup>8</sup>, and Benjamin Poulter<sup>9</sup>

5 <sup>1</sup>NASA Ames Research Center, Moffett Field, CA 94035, USA

6 <sup>2</sup>NASA Postdoctoral Program administered by Universities Space Research Association, Columbia, MD 21046, USA

7 <sup>3</sup>California State University, Monterey Bay, CA 93955, USA

8 <sup>4</sup>NOAA Earth System Research Laboratory, Global Monitoring Division, Boulder, CO 80305-3337, USA

9 <sup>5</sup>Cooperative Institute for Research in the Atmosphere, Colorado State University, Ft. Collins, CO 80521, USA

10 <sup>6</sup>Department of Atmospheric Science, Colorado State University, Fort Collins, CO 80523, USA

11 <sup>7</sup>Department of Mechanical Engineering, University of Colorado at Boulder, Boulder, CO 80309, USA

12 <sup>8</sup>Jet Propulsion Laboratory, California Institute of Technology, Pasadena, CA 91109, USA

13 <sup>9</sup>NASA Goddard Space Flight Center, Greenbelt, MD 20771, USA

14 *Correspondence to:* Sajeev Philip ([philip.sajeev@gmail.com](mailto:philip.sajeev@gmail.com)) and Matthew S. Johnson ([matthew.s.johnson@nasa.gov](mailto:matthew.s.johnson@nasa.gov))

15 **Abstract.** This study assesses the impact of different state-of-the-science global biospheric CO<sub>2</sub> flux models, when applied as prior  
16 information, on inverse modeling “top-down” estimates of terrestrial CO<sub>2</sub> fluxes obtained when assimilating Orbiting Carbon  
17 Observatory 2 (OCO-2) observations. This is done with a series of Observing System Simulation Experiments (OSSEs) using  
18 synthetic CO<sub>2</sub> column-average dry air mole fraction (XCO<sub>2</sub>) retrievals sampled at the OCO-2 satellite spatio-temporal frequency.  
19 The OSSEs used the four-dimensional variational (4D-Var) assimilation system with the GEOS-Chem global chemical transport  
20 model (CTM) to estimate CO<sub>2</sub> net ecosystem exchange (NEE) fluxes using synthetic OCO-2 observations. The impact of biosphere  
21 models in inverse model estimates of NEE is quantified by conducting OSSEs using the NASA-CASA, CASA-GFED, SiB-4 and  
22 LPJ models as prior estimates and using NEE from the multi-model ensemble mean of the Multiscale Synthesis and Terrestrial  
23 Model Intercomparison Project as the “truth”. Results show that the assimilation of simulated XCO<sub>2</sub> retrievals at OCO-2 observing  
24 modes over land results in posterior NEE estimates which generally reproduce “true” NEE globally and over terrestrial TransCom-  
25 3 regions that are well-sampled. However, we find larger spread among posterior NEE estimates, when using different prior NEE  
26 fluxes, in regions and seasons that have limited OCO-2 observational coverage and a large range in “bottom-up” NEE fluxes.  
27 Posterior NEE estimates had seasonally-averaged posterior NEE standard deviation (SD) of ~10% to ~50% of the multi-model-  
28 mean NEE for different TransCom-3 land regions with significant NEE fluxes (regions/seasons with a NEE flux  $\geq 0.5$  PgC yr<sup>-1</sup>).  
29 On a global average, the seasonally-averaged residual impact of the prior model NEE assumption on posterior NEE spread is ~10-  
30 20% of the posterior NEE mean. Additional OCO-2 OSSE simulations demonstrate that posterior NEE estimates are also sensitive  
31 to the assumed prior NEE flux uncertainty statistics, with spread in posterior NEE estimates similar to those when using variable  
32 prior model NEE fluxes. In fact, the sensitivity of posterior NEE estimates to prior error statistics was larger compared to prior  
33 flux values in some regions/times of the Tropics and Southern Hemisphere where sufficient OCO-2 data was available and large  
34 differences between the prior and “truth” were evident. Overall, even with the availability of dense OCO-2 data, noticeable residual  
35 differences (up to ~20-30% globally and 50% regionally) in posterior NEE flux estimates remain that were caused by the choice  
36 of prior model flux values and the specification of prior flux uncertainties.



## 1 Introduction

Carbon dioxide (CO<sub>2</sub>) is the most important greenhouse gas (GHG) contributing to climate change on a global scale (IPCC, 2014). The anthropogenic emission of CO<sub>2</sub>, primarily from fossil fuel usage, has led to average global CO<sub>2</sub> mixing ratios reaching historically high levels of > 400 parts per million (ppm) (Seinfeld and Pandis, 2016). In addition to fossil fuel emissions, the processes involved in the exchange of carbon between the atmosphere and terrestrial biosphere are a major factor controlling atmospheric concentrations of CO<sub>2</sub> (e.g., Schimel et al., 2001) with an estimated global biosphere sink of ~3.0 PgC yr<sup>-1</sup> (Le Quééré et al., 2018). However, current estimates of regional-scale atmosphere-terrestrial biosphere CO<sub>2</sub> exchange have large uncertainties (Schimel et al., 2015). “Bottom-up” techniques typically simulate the atmosphere-terrestrial biosphere exchange based on our understanding of these complex exchange processes and by constraining these estimates with remote-sensing inputs and limited measurements available for evaluation. Previous studies inter-comparing several of the most commonly used biospheric flux models (Heimann et al., 1998, Huntzinger et al., 2012; Sitch et al., 2015; Ott et al., 2015; Ito et al., 2016) and multi-model ensemble integration projects (Schwalm et al., 2015) reveal a large spread among global/regional “bottom-up” terrestrial biospheric flux estimates and the sub-components such as ecosystem primary production and respiration (Huntzinger et al., 2012).

An alternate approach to estimate biospheric CO<sub>2</sub> fluxes is through “top-down” estimation techniques using inverse models with highly accurate in situ data (e.g., Baker et al., 2006b) or dense and globally distributed satellite data (e.g., Chevallier et al., 2005). The Orbiting Carbon Observatory-2 (OCO-2) satellite, launched in 2014, is the space-borne sensor with the finest resolution and highest sensitivity of CO<sub>2</sub> in atmospheric boundary layer to date (Crisp et al., 2017; Eldering et al., 2017a). Studies applying OCO-2 retrievals revealed the ability to investigate novel aspects of the carbon cycle (e.g., Eldering et al., 2017b; Liu et al., 2017), however, the “top-down” estimates of surface CO<sub>2</sub> fluxes from numerous inverse modeling systems, using identical OCO-2 observations, show differences among optimized/posterior regional CO<sub>2</sub> fluxes (Crowell et al., in prep). Previous studies investigating CO<sub>2</sub> flux inversions (e.g., Peylin et al., 2013; Chevallier et al., 2014; Houweling et al., 2015) suggest that this spread among optimized CO<sub>2</sub> flux estimates could be due to numerous factors, such as the accuracy and precision of observation data (Rödenbeck et al., 2006), imperfect observation coverage (Liu et al., 2014; Byrne et al., 2017), data density (Law et al., 2003; Rödenbeck et al., 2003) and poorly characterized measurement error covariance (Law et al., 2003; Takagi et al., 2014). Variations in inverse estimation setups between modeling groups, such as model transport (Chevallier et al., 2010; Houweling et al., 2010; Basu et al., 2018) and inversion methods (Chevallier et al., 2014; Houweling et al., 2015), could also lead to inter-model spread in posterior estimates.

In addition to the variables listed above, the assumed prior fluxes and the associated prior error covariance can also impact “top-down” global/regional CO<sub>2</sub> flux estimates (e.g., Gurney et al., 2003). Gurney et al. (2003) assessed the sensitivity of CO<sub>2</sub> flux inversions to the specification of prior flux uncertainty and found that the posterior estimates were sensitive to the prior fluxes over regions with limited in situ observations. In addition, Wang et al. (2018) found that optimal CO<sub>2</sub> flux allocation over land versus ocean, using satellite and/or in situ data assimilations, is sensitive to the specification of prior flux uncertainty. Furthermore, Chevalier et al. (2005) and Baker et al. (2006a; 2010) highlighted the importance of accurate assumptions of prior flux uncertainty by conducting four-dimensional variational (4D-Var) assimilation of satellite column retrievals of CO<sub>2</sub>. However, to date, there are no controlled experimental studies to isolate and quantitatively assess the impact of assumed prior fluxes and prior uncertainty to inverse estimates of biospheric CO<sub>2</sub> fluxes using satellite observations.

Therefore, during this study we conduct a series of controlled experiments to quantitatively assess the impact of assumed prior fluxes and prior uncertainty on global and regional CO<sub>2</sub> inverse model flux estimates when assimilating OCO-2 data. In order to achieve this, a series of Observing System Simulation Experiments (OSSEs) are conducted using synthetic OCO-2 observations in the GEOS-Chem 4D-Var assimilation system, with four different prior “bottom-up” NEE CO<sub>2</sub> flux estimates. Section 2 of this



1 study describes the methods applied during this work including models and model input, synthetic OCO-2 data and the inversion  
2 technique applied in the OSSEs. Section 3 presents the forward and inverse model results of simulated atmospheric CO<sub>2</sub>  
3 concentrations and inferred posterior flux estimates. Finally, our concluding remarks and discussion are described in Section 4.

## 4 **2 Methods**

5 To quantify the impact of prior model NEE predictions on posterior estimates of biospheric CO<sub>2</sub> fluxes, a series of CO<sub>2</sub> forward  
6 and inverse model simulations were conducted with four different state-of-the-science biosphere models. OSSE simulations were  
7 designed to isolate the differences in posterior NEE estimates caused by the selection of prior model biospheric CO<sub>2</sub> fluxes and  
8 uncertainties when assimilating OCO-2 observations. The OSSE framework, input variables, inversion technique and analysis  
9 method are presented below.

### 10 **2.1 Prior NEE fluxes**

11 NEE is the net difference of gross primary production (GPP) and total ecosystem respiration ( $R_e$ ), which itself is the sum of  
12 autotrophic respiration ( $R_a$ ) and heterotrophic respiration ( $R_h$ ). NEE, estimated by terrestrial biospheric CO<sub>2</sub> flux models, is  
13 commonly applied in CTMs to simulate atmosphere-terrestrial biosphere carbon exchange. Many biosphere carbon models  
14 estimate GPP and  $R_e$ , however, some models simulate net primary productivity (NPP), which is defined as the difference between  
15 GPP and  $R_a$ . In this study, we apply year-specific NEE fluxes calculated from four state-of-the-science biosphere models: 1) NASA  
16 Carnegie Ames Stanford Approach (NASA-CASA), 2) CASA-Global Fire Emissions Database (CASA-GFED), 3) Simple-  
17 Biosphere model version 4 (SiB-4) and 4) Lund-Potsdam-Jena (LPJ). It should be noted that the prior biosphere models used in  
18 this study include only NEE and a single dataset for wild fire and fuel wood burning CO<sub>2</sub> emissions was added separately (see  
19 Sect. 2.3). The models applied during this study represent a range of diagnostic approaches, from models predicting biospheric  
20 CO<sub>2</sub> fluxes using remotely-sensed data (e.g., Fraction of Absorbed Photosynthetically Active Radiation, Leaf Area Index,  
21 Normalized Difference Vegetation Index) to fully prognostic models unconstrained by observations. In addition, we selected both  
22 balanced/neutral (SiB-4) and non-balanced (NASA-CASA, CASA-GFED, LPJ) biospheric fluxes in our OSSEs in order to  
23 represent the range of prior models currently being used in CO<sub>2</sub> inversion modeling studies.

24 CASA is an ecosystem model predicting NPP based on light use efficiency and  $R_h$  based on soils/plant production  
25 information (Potter et al., 1993; 2012b). The NASA-CASA model is a version of the original CASA model (Potter et al., 1993)  
26 currently being developed at NASA Ames Research Center (Potter et al., 2003; 2007; 2009; 2012a; 2012b). NASA-CASA  
27 specifically utilizes data on global vegetation cover (enhanced vegetation index, surface solar irradiance data) and land disturbances  
28 retrieved from the NASA Moderate Resolution Imaging Spectroradiometer (MODIS) satellite (Potter et al., 2012b). In addition to  
29  $R_h$ , NASA-CASA includes redistributed crop harvest CO<sub>2</sub> emissions to the atmosphere (Potter et al., 2012b). The CASA-GFED  
30 model is a different version of the original CASA model and is described in Randerson et al. (1996) with subsequent versions  
31 being described in recent literature (van der Werf et al., 2004; 2006; 2010). NASA-CASA and CASA-GFED differ in the use of  
32 input parameters and some of the parameterizations (see Ott et al. (2015) for further description).

33 The SiB-4 model was developed at Colorado State University (Sellers et al., 1986; Denning et al., 1996) with details of  
34 the newest versions described in Haynes et al. (2013). This model is a mechanistic, prognostic land surface model that integrates  
35 heterogeneous land cover, environmentally responsive prognostic phenology, dynamic carbon allocation and cascading carbon  
36 pools from live biomass to surface litter and soil organic matter (Haynes et al., 2013; Baker et al., 2013; Lokupitiya et al., 2009;  
37 Schaefer et al., 2008; Sellers et al., 1996). By combining biogeochemical, biophysical and phenological processes, SiB-4 predicts  
38 vegetation and soil moisture states, land surface energy and water budgets and the terrestrial carbon cycle. Rather than relying on



1 satellite input data, SiB-4 fully simulates the terrestrial carbon cycle by using the carbon fluxes to determine the above and below-  
2 ground biomass, which in turn feed back to impact carbon assimilation and respiration. Similar to NASA-CASA, the SiB4 model  
3 redistributes crop harvest CO<sub>2</sub> emission to the atmosphere. Note that we use a balanced (neutral) biospheric NEE flux (balanced  
4 biosphere for the 1998-2017 time period) for the SiB-4 model.

5 The LPJ model is a process-based dynamic global vegetation model (Sitch et al., 2003; Polter et al., 2014). The LPJ-wsl  
6 dynamic global vegetation model (Sitch et al., 2003) was used to simulate NEE using meteorological data from the Climate  
7 Research Unit (Harris et al., 2013). LPJ is fully prognostic, meaning that the establishment, growth and mortality of vegetation are  
8 represented by first-order physiological principles. The model includes nine plant functional types distinguished by their  
9 phenology, photosynthetic pathway and physiognomy. Phenology status is determined daily and photosynthesis is estimated using  
10 a modified Farquhar scheme (Haxeltine and Prentice, 1996). NPP is calculated from photosynthesis after accounting for R<sub>a</sub> and  
11 reproductive allocation. The LPJ-wsl model has been evaluated in several benchmarking activities for stocks and fluxes (Peng et  
12 al., 2015; Sitch et al., 2015).

13 In order to provide a “true” NEE flux for the OSSEs conducted in this study (Sect. 2.4), we use the multi-model ensemble  
14 NEE mean from the Multiscale Synthesis and Terrestrial Model Intercomparison Project (MsTMIP) (Huntzinger et al., 2013; 2018;  
15 Fisher et al., 2016a; 2016b). The MsTMIP NEE fluxes are from a weighted ensemble mean of 15 biosphere models (Schwalm et  
16 al., 2015) for the year 2010. Here we apply the MsTMIP data for year 2010 as the “truth” with year-specific prior model predictions  
17 for 2015. This procedure is justified in our case as within an OSSE framework there needs to be a difference between “true” and  
18 prior fluxes, as long as the “true” values are realistic in nature. The MsTMIP ensemble NEE mean represents a summary over all  
19 15 models which smooths out errors particular to any given model. This “true” NEE flux is used to produce the synthetic OCO-2  
20 observations applied in this study (described further in Sect. 2.4.3).

21 The four prior and the “true” NEE fluxes were regridded from their native horizontal resolutions to the grid resolution of  
22 the inverse model simulations (4.0° latitude × 5.0° longitude). The MsTMIP NEE fluxes are provided as 3-hourly averages and  
23 the four year-specific prior models were provided as monthly-mean GPP or NPP and R<sub>c</sub> or R<sub>h</sub>. Therefore, we imposed diurnal  
24 (hourly) and daily variability to these four prior models following the approach in CarbonTracker CT2016  
25 (<http://carbontracker.noaa.gov>), which is based on Olsen and Randerson (2004). This hourly/daily NEE variability for each prior  
26 model was calculated using the downward solar radiation flux and 2-meter air temperature data from the GEOS-FP (Goddard Earth  
27 Observing System Model, Version 5 "Forward Processing") meteorological product and monthly-averaged GPP and R<sub>h</sub> from the  
28 respective model. We allow the “true” and prior models to have different diurnal variability in order to represent a realistic scenario,  
29 as prior models will differ some from the actual diurnal variability of NEE in nature. Table 1 shows the global annual NEE flux  
30 estimates for the four prior models and the “truth”. From this table it can be seen that the MsTMIP product shows a strong annual  
31 global sink of -4.31 PgC yr<sup>-1</sup>. NASA-CASA and CASA-GFED predict a global sink of ~2 PgC yr<sup>-1</sup> and differ by ~0.6 PgC yr<sup>-1</sup>.  
32 SiB-4 NEE predicts a source of ~1 PgC yr<sup>-1</sup> and the LPJ model predicts a strong sink of ~5.5 PgC yr<sup>-1</sup>. Section 3.1 further describes  
33 the spatio-temporal differences of the NEE fluxes between these four prior models and the “truth”.

## 34 2.2 GEOS-Chem model

35 The GEOS-Chem chemical transport model (CTM) (<http://geos-chem.org>; Bey et al., 2001) used in this study has the capability to  
36 run forward CO<sub>2</sub> simulations (Suntharalingam et al., 2004; Nassar et al., 2010) and corresponding adjoint model calculations  
37 (Henze et al., 2007; Liu et al., 2014). In this study, we use the GEOS-Chem adjoint version 35, which is compatible with version  
38 8-02 of the GEOS-Chem forward model. Liu et al. (2014) tested the accuracy of the GEOS-Chem CO<sub>2</sub> adjoint system, which has  
39 been used for several CO<sub>2</sub> inverse modeling studies (e.g., Liu et al., 2017; Bowman et al., 2017; Deng et al., 2014). The model is



1 driven with assimilated meteorological fields from the GEOS-FP model of the NASA Global Modeling Assimilation Office  
2 (GMAO). The GEOS-FP meteorology fields have a native horizontal resolution of  $0.25^\circ \times 0.3125^\circ$  and 72 native hybrid sigma-  
3 pressure vertical levels from the Earth's surface to 0.01 hPa. We conduct simulations with a coarser spatial resolution ( $4.0^\circ \times 5.0^\circ$ )  
4 with 47 reduced vertical levels to attain reasonable computational efficiency.

### 5 **2.3 Non-NEE CO<sub>2</sub> fluxes**

6 To simulate concentrations of atmospheric CO<sub>2</sub>, we used several land and ocean CO<sub>2</sub> flux inventories in addition to the NEE  
7 estimates from the prior biosphere models (global annual budgets listed in Table 1). This study used the year-specific fossil fuel  
8 and cement production inventory from the Open-source Data Inventory for Anthropogenic CO<sub>2</sub> (ODIAC-2016) developed by Oda  
9 et al. (2018). Following the approach of Nassar et al. (2013), the monthly ODIAC-2016 inventory is converted from the native  
10 temporal variability into diurnal (hourly) and weekday/weekend variability (courtesy: Sourish Basu and the OCO-2 Science Team).  
11 Wild fire emissions and fuel wood burning emissions were taken from the 3-hourly varying Global Fire Emissions Database  
12 (GFED3) database. Shipping emissions are from the International Comprehensive Ocean-Atmosphere Data Set (ICOADS)  
13 (Corbett and Koehler, 2003; 2004) and aviation emissions are from Aviation Emissions Inventory Code (AEIC) inventory (Olsen  
14 et al., 2013). We used 3D chemical production of CO<sub>2</sub> from the oxidation of carbon monoxide, methane and non-methane volatile  
15 organic compounds (Nassar et al., 2010). The shipping, aviation and 3D chemical source are climatological and are taken from the  
16 Bowman (2017) dataset. To simulate oceanic CO<sub>2</sub> fluxes, we apply the year-specific 3-hourly posterior estimates from the  
17 CarbonTracker 2016 (CT2016) model constrained with in situ data (Peters et al., 2007; <http://carbontracker.noaa.gov>). All emission  
18 inventories, besides NEE fluxes, are kept constant between the different inverse model simulations.

### 19 **2.4 Observing System Simulation Experiments (OSSEs)**

#### 20 **2.4.1 OSSE framework**

21 This study conducted several OSSEs to assess the impact of prior biospheric CO<sub>2</sub> models and associated prior uncertainty  
22 specifications on posterior estimates of NEE when assimilating OCO-2 data. To assess the impact of prior fluxes, we conduct four  
23 baseline OSSEs (using the four prior biosphere models) assimilating synthetic land nadir (LN) and land glint (LG) observations  
24 together, plus an additional four OSSEs using just ocean glint (OG) observations. These OSSE simulations were designed in such  
25 a way that the differences in posterior NEE estimates are due solely to the choice of prior biospheric flux (e.g., identical initial  
26 atmospheric CO<sub>2</sub> conditions, non-NEE fluxes, OCO-2 sampling frequency, observational data uncertainty, etc.). Furthermore, to  
27 assess the impact of prior uncertainty specifications, we conduct two additional OSSEs (in addition to our baseline prior uncertainty  
28 assumption described in Sect. 2.4.5) with synthetic LN and LG observations using prior error set uniformly to 10% and 100% of  
29 a particular prior NEE flux (CASA-GFED). Table 2 shows the summary of OSSEs conducted for this study. During all OSSE  
30 simulations NEE and oceanic CO<sub>2</sub> fluxes are optimized, with all other sources kept constant, in order to be consistent with the  
31 methods commonly used by inverse modeling systems focused on estimating NEE. We optimize oceanic fluxes together with NEE,  
32 although the same ocean fluxes were used for the “truth” and the prior in all OSSE simulations (Sect. 2.3) for simplicity and  
33 because the terrestrial NEE fluxes are the focus of this work. It is noteworthy that the assimilation of land or ocean data in fact do  
34 not produce substantial deviations from the “truth” over the TransCom-3 oceanic regions (Fig. S1). For all OSSE simulations, an  
35 assimilation window of 18 months covering the period from August 1, 2014 to January 31, 2016 was applied. NEE/oceanic fluxes  
36 are optimized for every month of the assimilation window at each surface grid box in the GEOS-Chem model. The analysis of  
37 prior and posterior NEE fluxes is for all months in 2015, treating the other months as spin-up and spin-down periods.



#### 1 2.4.2 Initial CO<sub>2</sub> concentrations

2 We use identical initial atmospheric concentrations of CO<sub>2</sub> at August 1, 2014 for: 1) the GEOS-Chem forward model simulations  
3 generating synthetic XCO<sub>2</sub> using the “true” NEE fluxes (Sect. 2.4.3) and 2) for all the OSSEs using variable prior biosphere model  
4 predictions. The initial CO<sub>2</sub> concentrations were generated by running the GEOS-Chem forward model for two years using the  
5 “true” MsTMIP NEE and other non-NEE CO<sub>2</sub> sources. The restart file used for this two year forward model run was taken from  
6 an earlier GEOS-Chem model simulation constrained with in situ observations (personal communication from Ray Nassar) in order  
7 to represent a realistic initial condition.

#### 8 2.4.3 Synthetic OCO-2 retrievals

9 In this study, we used synthetic satellite data that is directly representative of version 8 of the OCO-2 product. The OCO-2 satellite  
10 sensor is in sun-synchronous polar orbit with a repeat cycle of 16 days and a local over-pass time in the early afternoon (Crisp et  
11 al., 2017). OCO-2 has three different viewing modes: soundings over land from LN and LG and over oceans from OG. The  
12 algorithm of O’Dell et al. (2012) is used to retrieve column-average dry air mole fraction of CO<sub>2</sub> (XCO<sub>2</sub>) and other retrieval  
13 variables. OCO-2 XCO<sub>2</sub> is retrieved using the following equation using a prior CO<sub>2</sub> vertical profile ( $\mathbf{c}_a$ ) and prior CO<sub>2</sub> column  
14 (XCO<sub>2(a)</sub>) value,

$$15 \quad XCO_2 = XCO_{2(a)} + \mathbf{a}^T(\mathbf{c} - \mathbf{c}_a) \quad (1)$$

16 where  $\mathbf{c}$  is the true profile of CO<sub>2</sub> concentrations,  $\mathbf{a}$  is the averaging kernel vector. The individual soundings of OCO-2 are at a  
17 fine-resolution (24 spectra per second with < 3 km<sup>2</sup> spatial resolution per sounding), leading to a very large data volume (Crisp et  
18 al., 2017). This level of detail is lost when the measurements are used in global inverse models with much coarser spatial resolution,  
19 with numerous individual OCO-2 soundings occur in a single model grid cell. In addition, each sounding does not really provide  
20 an independent piece of information to the inversion system due to spatial and temporal error correlations. Therefore, we use 10-  
21 sec averages of the individual XCO<sub>2</sub> soundings similar to those developed/described in Basu et al. (2018), however, from an  
22 updated version with file name: OCO2\_b80\_10sec\_WL04\_GOOD\_v2.nc. This 10-sec data contains averages of retrievals with a  
23 “GOOD” quality flag and Warn Level from 1 to 4. Note that in this study we do not use actual retrieved 10-sec XCO<sub>2</sub> values for  
24 our OSSEs, however, synthetic XCO<sub>2</sub> data were generated corresponding to the spatio-temporal sampling frequency of version 8  
25 OCO-2 10-sec data. The synthetic 10-sec XCO<sub>2</sub> data is calculated with the CO<sub>2</sub> concentration profile simulated using the GEOS-  
26 Chem forward model (using MsTMIP as the NEE flux model). In this manner we produced synthetic XCO<sub>2</sub> data that is  
27 representative of the “true” atmosphere corresponding to the “true” NEE fluxes used in this study. We archive these synthetic  
28 XCO<sub>2</sub> data and applied them for all OSSEs conducted.

#### 29 2.4.4 Inverse modeling approach

30 The transport of atmospheric CO<sub>2</sub> is simulated using GEOS-Chem along with prescribed surface fluxes as input data (see Table  
31 1). Subsequently, the GEOS-Chem 4D-Var inverse modeling system assimilates synthetic OCO-2 XCO<sub>2</sub> data to estimate the  
32 posterior/optimized monthly-mean NEE and oceanic fluxes at each surface grid of the model. The GEOS-Chem adjoint system  
33 applies the L-BFGS numerical optimization algorithm with a no-bound option (Liu and Nocedal, 1989). Posterior monthly-  
34 averaged NEE/oceanic fluxes ( $\mathbf{x}$ ) are inferred for each surface model grid by optimizing a vector of scaling factors  $\sigma_j$  for the  $j^{\text{th}}$   
35 model grid,

$$36 \quad x_j = \sigma_j x_{a,j} \quad (2)$$



1 where  $\mathbf{x}_a$  represents the monthly-mean prior NEE/oceanic fluxes. Scaling factors are assumed to be unity at the first iteration (that  
2 is, prior NEE flux itself is used). The inversion system, as described below, optimizes the scaling factor applied to the monthly-  
3 mean fluxes and the posterior scaling factors are then used to scale prior fluxes to infer posterior CO<sub>2</sub> fluxes.

4 For each iteration, the inversion system uses the forward model simulated profiles of CO<sub>2</sub> concentrations mapped to OCO-  
5 2 retrieval levels ( $\mathbf{f}(\mathbf{x})$ ) in each model grid in order to compare with the synthetic OCO-2 observations ( $\mathbf{y}$ ). The observation operator  
6 ( $\mathbf{M}$ ) represents the model simulated XCO<sub>2</sub> corresponding to each synthetic OCO-2 retrieval,

$$7 \quad \mathbf{M} = \mathbf{M}_a + \mathbf{a}^T (\mathbf{f}(\mathbf{x}) - \mathbf{y}_a) \quad (3)$$

8 where  $\mathbf{M}_a$  is the prior XCO<sub>2</sub> used in the retrieval of the OCO-2 XCO<sub>2</sub> product and  $\mathbf{y}_a$  is the corresponding prior profile of CO<sub>2</sub>  
9 concentrations assumed in the retrieval. The optimization approach used in this work defines the 4D-Var cost function ( $\mathcal{J}$ ) as,

$$10 \quad \mathcal{J}(\boldsymbol{\sigma}) = \frac{1}{2} \sum_i (\mathbf{M}_i - \mathbf{y}_i)^T \mathbf{R}_i^{-1} (\mathbf{M}_i - \mathbf{y}_i) + \frac{1}{2} (\boldsymbol{\sigma} - \boldsymbol{\sigma}_a)^T \mathbf{P}^{-1} (\boldsymbol{\sigma} - \boldsymbol{\sigma}_a) \quad (4)$$

11 where  $\mathbf{y}_i$  is the vector of synthetic OCO-2 XCO<sub>2</sub> data across the assimilation window, with ‘i’ being the number of XCO<sub>2</sub> data.  
12 Furthermore,  $\mathbf{R}$  and  $\mathbf{P}$  are the observational error covariance matrix and prior error covariance matrix, respectively.

#### 13 2.4.5 Prior flux uncertainty

14 For a perfect optimization, the prior error covariance matrix ( $\mathbf{P}$ ) assumed in the inversion should equal the uncertainty of the prior  
15 model used. However, the estimation of prior error statistics is a challenging task due to the lack of flux evaluation data. Previous  
16 studies have used a range of techniques to characterize prior error covariance: by developing the full error covariance matrix with  
17 assumed error correlations (Basu et al., 2013), based on a fraction of heterotrophic respiration (Basu et al., 2018), conducting  
18 Monte Carlo simulations (Liu et al., 2014), using standard deviations and absolute differences between several different prior flux  
19 models (Baker et al., 2006a; 2010) and applying globally uniform prior flux uncertainty values to satisfy the posterior  
20  $\chi^2$  (normalized cost function) = 1 criteria (Deng et al., 2014). During this study, a  $1\sigma$  standard deviation (SD) of the four prior  
21 biosphere models (see Sect. 3.1 for the description of SD values) is considered to be the measure of uncertainty in the prior  
22 knowledge of “bottom-up” model predicted biospheric CO<sub>2</sub> fluxes. The SD of the four prior NEE estimates is applied in the prior  
23 error covariance matrix and no spatial or temporal correlations are taken in to account. This assumption is reasonable as optimized  
24 fluxes are at coarse spatio-temporal scales (monthly mean fluxes at horizontal resolutions of > 400 km<sup>2</sup>) and is representative of  
25 the majority of inverse modeling studies assimilating CO<sub>2</sub> satellite data (e.g., Baker et al., 2010; Liu et al., 2014; Deng et al., 2014).  
26 Finally, since the inverse modeling system applied in this work optimizes scaling factors, we use the square of the fractional prior  
27 error in the  $\mathbf{P}$  matrix, where the fractional error is calculated for each individual prior model as the SD of the four prior models  
28 divided by the absolute value of the NEE magnitude. For generating prior error for the oceanic fluxes, we follow the same method  
29 we adopted for generating prior errors in NEE. The SD of four different state-of-the-science oceanic CO<sub>2</sub> flux datasets (NASA-  
30 CMS CO<sub>2</sub> oceanic flux from Bowman (2017), CarbonTracker 2016 prior ocean data (CT2016; <http://carbontracker.noaa.gov>),  
31 Takahashi et al. (2009) and Landschützer et al. (2016; 2017)) was calculated to generate prior error values.

#### 32 2.4.6 XCO<sub>2</sub> uncertainty

33 As described in Sect. 2.4.3, the synthetic XCO<sub>2</sub> used in this study is calculated at the spatio-temporal sampling frequency of OCO-  
34 2 10-sec average dataset. Although we use synthetic XCO<sub>2</sub>, we apply the same observation error statistics generated with the actual  
35 OCO-2 XCO<sub>2</sub> 10-sec dataset in order to develop the observational error covariance matrix ( $\mathbf{R}$ ). The final observation error for the  
36 10-sec average data is generated as a quadratic sum of the retrieval error from individual OCO-2 soundings, 10-sec averaging error,  
37 and a ‘model representation error’ as described in Basu et al. (2018). Similar to prior error statistics, we neglect observation error  
38 correlations and assume a diagonal observational error covariance. No random perturbations were added to the synthetic XCO<sub>2</sub>



1 used in this study, as the goal of this work was not to quantify the analytical posterior flux uncertainty but instead was aimed to  
2 analyze the spread among posterior NEE estimates. We note that other inverse modeling groups assimilating OCO-2 data also do  
3 not add random perturbations to the data and use the same error statistics generated along with the OCO-2 10-sec product that are  
4 applied in this study (e.g., Basu et al., 2018; Crowell et al., in prep). During this study the square of the observation error for the  
5 10-sec average data was applied as the diagonal in the  $\mathbf{R}$  matrix. From our initial OSSE tests it was determined that the use of 10-  
6 sec error statistics led to posterior  $\chi^2$  (normalized cost function) values that were much lower than unity. Therefore, we divided  
7 the 10-sec error values uniformly by a factor of 5 to approximately satisfy the  $\chi^2 = 1$  criteria for all the OSSEs. This deflation  
8 procedure reduced the average 10-sec observational error values for LN+LG (OG) data from  $\sim 1.5$  ( $\sim 0.9$ ) ppm to  $\sim 0.3$  ( $\sim 0.2$ ) ppm.  
9 These procedures give more confidence to the observational data and lead to results in this study which can be assumed as the  
10 lower limit of the impact of prior model flux and uncertainty statistics in inverse model estimates.

#### 11 2.4.7 Evaluation of OSSE results

12 During this study, the posterior NEE values from the OSSEs are compared to the “true” fluxes to assess accuracy and also inter-  
13 compared to assess the spread in posterior estimates due to the assumed prior NEE and prior error statistics. The primary statistical  
14 parameters used to evaluate the spread in posterior NEE fluxes are the SD (hereafter the term “spread” will be used to represent  
15 SD) and range (difference between maximum and minimum in NEE). The SD/spread and range of posterior NEE estimates, when  
16 using the different prior models, will provide an understanding of the spatio-temporal residual impact of the prior models in “top  
17 down” estimates of global/regional NEE fluxes when assimilating OCO-2 data.

18 In order to evaluate the spatio-temporal variability of prior and posterior regional NEE fluxes, we aggregate individual  
19 model grids to The Atmospheric Tracer Transport Model Intercomparison Project-3 (TransCom-3) land regions (TransCom-3  
20 regions illustrated in Fig. S2). To further interpret the OSSE results, we produce additional classifications of three broad  
21 hemisphere-scale TransCom-3 land regions: Northern Land (NL), Tropical Land (TL) and Southern Land (SL). TL includes  
22 Tropical South America, North Africa and Tropical Asia; SL includes South American Temperate, South Africa and Australia;  
23 and NL includes the other five land regions. The evaluation of SD and range of prior model and posterior/optimized NEE fluxes  
24 were calculated for the 11 individual TransCom-3 regions, for the three hemisphere-scale TransCom-3 regions and globally.  
25 Throughout the manuscript, seasonally-averaged prior and posterior NEE fluxes will be discussed and these seasons are presented  
26 with respect to the Northern Hemisphere.

#### 27 2.4.8 Pseudo data assimilations

28 In order to test our OSSE framework, we first run four “pseudo” experiments by conducting inverse modeling studies using  
29 “pseudo” surface observations. These test OSSE simulations were conducted for five-month assimilation windows for two separate  
30 seasons (November 2014 to March 2015 (analysis for winter, DJF) and May 2015 to September 2015 (analysis for summer, JJA))  
31 using all four prior model NEE values separately. Simulated hourly concentrations of  $\text{CO}_2$  for all surface grids of GEOS-Chem are  
32 taken as “pseudo” surface observations. In order to check whether the model framework can converge to the “truth”, a simple  
33 controlled experiment was performed assuming a very small observational data uncertainty (0.001%) and with the prior flux  
34 uncertainty set equal to the absolute magnitude of the “truth” - prior NEE (divided by the absolute value of the NEE magnitude for  
35 that respective prior model). The robustness of the flux inversions conducted in the subsequent sections is validated by the results  
36 of these “pseudo” tests. Figure S3 shows the results of the four “pseudo” tests using the four different NEE flux model predictions  
37 as the prior information. From this figure it is apparent that, regardless of the prior NEE assumed, posterior NEEs were able to  
38 reproduce the “truth” with near perfect accuracy for all TransCom-3 regions, with the range between the posterior NEEs typically



1 approaching  $\sim 0$  PgC yr<sup>-1</sup>. This test also demonstrates that a “perfect” assimilation (using uniform and dense surface data coverage,  
2 highly accurate data and known/loose prior uncertainty) is almost insensitive to the prior assumed. Having tested the robustness of  
3 our inversion setup, we feel confident in presenting the output from our OSSE framework, using synthetic OCO-2 remote-sensing  
4 data, in the following sections.

### 5 **3. Results and discussion**

#### 6 **3.1 Prior NEE fluxes**

7 Figure 1 shows the seasonally-averaged multi-model-mean and SD of the NEE fluxes from the four prior biosphere models used  
8 in the OSSE simulations (individual prior model and “true” seasonally-averaged NEE fluxes are displayed in Fig. S4). This figure  
9 shows the main features of NEE that are expected, such as the Northern Hemispheric fall/winter maximum in  $R_e$  and summer  
10 maximum in GPP due to the seasonality of photosynthesis and respiration. Figure 1 also shows the spread of the four prior model  
11 fluxes (used as prior uncertainty), which is typically highest over the Temperate regions of the Northern Hemisphere in the spring  
12 and summer and high in the Tropical regions during all seasons (the left panel of Figure S5 shows a spatial map of the corresponding  
13 range of the four prior model fluxes). Furthermore, Fig. S6 shows the time-series of monthly-mean prior NEE fluxes, and the  
14 corresponding prior error uncertainty (error bars), for the individual prior models. From this figure it can be seen that the  $1\sigma$  prior  
15 uncertainties for the global land are  $\sim 50$ - $70\%$  of the total NEE for the different prior models, with variability among other  
16 TransCom-3 land regions.

17 Table 3 displays the statistics of the prior NEE multi-model-mean and SD and range for the 11 individual TransCom-3  
18 land regions. The SD values for prior NEE fluxes range from  $\sim 20\%$  to frequently  $> 100\%$  of the multi-model NEE mean for  
19 different regions/seasons with significant NEE fluxes (hereafter this refers to regions/seasons with NEE flux  $\geq 0.5$  PgC yr<sup>-1</sup>). When  
20 comparing the magnitude of NEE between the four prior models, it can be seen from this table that the range in NEE values are  
21 large in some regions (up to 6 PgC yr<sup>-1</sup>). In general, all regions/seasons tend to have at least an  $\sim 1$  PgC yr<sup>-1</sup> range among the four  
22 prior models, indicating the large diversity in NEE predicted by current “bottom-up” biosphere models (Table 3). Figure S6 shows  
23 the time-series of monthly-mean NEE for individual prior models averaged over the globe, hemispheric-scale land regions (NL,  
24 TL, SL) and the 11 individual TransCom-3 land regions. It can be seen from this figure that the majority of the seasonality in the  
25 global NEE flux is controlled by the NL regions. Figure S6 also shows that the spread in prior NEE fluxes in general is larger for  
26 TL and SL regions compared to the NL, except for the North American Temperate region. Furthermore, when focusing on  
27 individual models, differences in NEE seasonality are evident. The impact of these differences among the four prior biospheric  
28 CO<sub>2</sub> flux models on simulated XCO<sub>2</sub> and posterior estimates of global/regional NEE fluxes is evaluated in the following sections.

#### 29 **3.2 Simulated XCO<sub>2</sub>**

30 Figure 2 shows the number of observations sampled in the OCO-2 LN and LG modes during the different seasons of 2015 summed  
31 in each model grid. Large spatio-temporal variability can be seen in the OCO-2 observation density, with the largest values over  
32 regions with minimal cloud coverage (e.g., desert regions of North/South Africa, Middle East, Australia, etc.). The opposite is true  
33 for many Tropical regions (e.g., Amazon, central Africa, Tropical Asia, etc.) where cloud occurrence is prominent and the number  
34 of OCO-2 observations is lowest. From Fig. 2 it can also be seen that the OCO-2 observation density has noticeable seasonality.  
35 For example, during the winter months low numbers of OCO-2 observations are made in the Northern Boreal regions and the  
36 largest amounts are observed during the summer. Furthermore, larger numbers of OCO-2 observations are made in the SL during  
37 the summer (JJA) compared to other seasons.



1           The seasonally-averaged multi-model-mean GEOS-Chem simulated XCO<sub>2</sub> using the four prior model NEE fluxes is  
2 shown in the right panel of Fig. 2. The most notable feature in this figure is the Northern Hemisphere seasonality, with higher  
3 XCO<sub>2</sub> concentrations in the winter months and lowest XCO<sub>2</sub> values in the growing seasons of the summer. Seasonality in model-  
4 predicted XCO<sub>2</sub> values is also evident in the TL and SL, with largest values in the autumn and lowest values in the spring. Figure  
5 S7 (left panel) shows the range of XCO<sub>2</sub> values simulated using the four prior model NEE fluxes. The differences between  
6 individual model simulations of XCO<sub>2</sub> values deviated among themselves by up to ~10 ppm. These large differences in XCO<sub>2</sub>  
7 values across the four different prior NEE flux models show that the choice of prior NEE has a large impact on simulated XCO<sub>2</sub>  
8 values.

### 9   **3.3 Optimized global NEE fluxes**

10 From Table 1 it can be seen that annual global mean posterior NEE flux, when using the different prior models and assimilating  
11 synthetic LN+LG OCO-2 XCO<sub>2</sub>, ranges from -4.11 to -4.36 PgC yr<sup>-1</sup>, which are generally close in magnitude to the “true” flux of  
12 -4.31 PgC yr<sup>-1</sup>. Although these posterior NEEs generally converged to the “truth”, there are some remaining differences, with an  
13 annual global mean posterior NEE range of 0.25 PgC yr<sup>-1</sup> (~6% of the multi-model-mean posterior NEE; Table 1). From the results  
14 of the OSSE simulations, it was found that the spread and range in XCO<sub>2</sub> simulated using the optimized posterior NEE fluxes was  
15 greatly reduced compared to the spread in XCO<sub>2</sub> simulated using prior NEE fluxes. This is evident from the right panel of Fig. S7  
16 where XCO<sub>2</sub> simulated using posterior NEE fluxes differ among themselves by < 0.5 ppm, which is greater than an order of  
17 magnitude lower, on average, than the spread among XCO<sub>2</sub> simulated using prior NEEs.

18           Figure S5 shows the spatial distribution of the range of prior and posterior NEEs. As expected, the range in optimized  
19 posterior NEE flux estimates starting from the four separate prior models was substantially reduced compared to the spread in prior  
20 NEE fluxes. However, the posterior NEE fluxes for individual surface grid boxes of the model still depict some residual range  
21 among the posteriors, with the largest residuals being found across South America and South Africa in all seasons and in Temperate  
22 regions of the Northern Hemisphere in the spring months. As shown in Fig. S5, the geographical pattern of the range of prior and  
23 posterior NEEs does not indicate any noticeable correlations. From comparing Figs. S5 and S7, it is apparent that the spread in  
24 posterior XCO<sub>2</sub> is significantly reduced in all regions of the globe compared to prior model simulations, however, while posterior  
25 NEE values are reduced compared to the prior, noticeable residual spread remains in some regions. This emphasizes the fact that  
26 the OSSEs successfully converge to match the synthetic OCO-2 XCO<sub>2</sub> values by optimizing NEE in different ways depending on  
27 the prior NEE model used. The following sections investigate the regional differences in posterior NEE estimates due to the residual  
28 impact of prior biospheric CO<sub>2</sub> flux predictions.

### 29   **3.4 Optimized regional NEE fluxes**

30 Figure 3 shows the seasonally-averaged “true”, prior and posterior NEE flux values for the 11 individual TransCom-3 land regions  
31 (with detailed statistics in Table 3 and monthly-mean time-series in Fig. S8). The first thing noticed from this figure is that all  
32 posterior NEE values, using variable priors, tend to reproduce the “truth” in most TransCom-3 land regions. From Fig. 3 it can  
33 also be seen that the assimilation of synthetic OCO-2 LN+LG XCO<sub>2</sub> retrievals resulted in a large reduction in the range among the  
34 four modeled NEE values (Table 3 shows the corresponding SD values). The reduction in the SD of NEE in most regions/seasons,  
35 calculated as  $100 \times (1 - (\text{posterior NEE SD})/(\text{prior NEE SD}))$  is generally > 70% and up to 98%. However, the range of seasonal  
36 mean posterior NEEs over individual TransCom-3 regions is still as large as 1.4 PgC yr<sup>-1</sup> when applying different prior NEE, with  
37 the largest ranges occurring in Northern Boreal regions (North America Boreal, Eurasian Boreal and Europe) in winter months.  
38 During the spring and summer months, regions in the TL (e.g., Tropical Asia) and SL (e.g., South American Temperate, South



1 Africa) have ranges in posterior NEEs up to  $\sim 0.5 \text{ PgC yr}^{-1}$ . The larger residual range among posterior NEE estimates for winter  
2 months in Northern Boreal regions is likely due to the insufficient OCO-2 observations during this time (see Fig. 2), while the  
3 larger range in the TL and SL regions is due to differences in the priors (see Fig. 1). This demonstrates that the impact from the  
4 prior model has regional and seasonal variability depending on: 1) the spatio-temporal flux variabilities inherent in prior NEEs and  
5 2) the observation density and coverage of synthetic OCO-2 data. Figure 3 and Table 3 show that the seasonally-averaged posterior  
6 NEE spread varies from  $\sim 10\%$  to  $\sim 50\%$  of the multi-model-mean for different TransCom-3 land regions with significant NEE  
7 fluxes. When evaluating this residual spread in posterior NEEs on a global average, seasonally-averaged values ranged from  $\sim 10\%$   
8 (JJA) to  $\sim 20\%$  (DJF) of the posterior NEE mean. These statistics reveal that the impact of prior models lead to a much larger  
9 spread/range for regional/seasonal posterior fluxes (up to  $\sim 50\%$ ) compared to annual global averaged values ( $6\%$ ). This emphasizes  
10 that while OCO-2 observations on average constrain global, hemispheric and regional biospheric fluxes, noticeable residual  
11 differences in posterior NEE flux estimates remain due to the choice of prior model values. Overall, the results of this evaluation  
12 suggest that when inter-comparing inverse model results assimilating similar OCO-2 observational data, differences in posterior  
13 NEE in regions with significant NEE fluxes could vary by up to  $\sim 50\%$  when using different prior flux assumptions.

### 14 3.5 Impact of prior uncertainty

15 Results of this study thus far have demonstrated the sensitivity of posterior NEE estimates to prior NEE flux assumptions. In this  
16 section, the sensitivity of posterior NEE estimates to the assumed prior uncertainty is tested, when assimilating synthetic OCO-2  
17 LN+LG XCO<sub>2</sub> observations. The general importance of prior uncertainty values is highlighted in the TL regions. In these regions  
18 the largest differences in prior models are calculated, thus largest prior uncertainty is assigned, resulting in larger deviations from  
19 the prior and posterior NEE spread similar to other TransCom-3 land regions (see Fig. 3). In order to quantify the sensitivity of  
20 posterior NEE to prior uncertainty statistics, a single prior NEE flux model (CASA-GFED) is applied in the OSSE framework,  
21 with variable prior flux uncertainty assumptions. Two additional OSSE simulations (in addition to the baseline simulations using  
22 the SD of the four prior models as the prior uncertainty; see right panel of Fig. 1 for SD maps) are performed using prior NEE  
23 magnitudes from CASA-GFED and setting the prior uncertainty uniformly as 10% and 100% of the CASA-GFED NEE values.  
24 Figure 4 shows the results of these additional OSSE simulations over the TransCom-3 land regions. From this figure it can be seen  
25 that the range of seasonal mean posterior NEEs over individual TransCom-3 regions vary from  $\sim 0.1$  to  $> 1 \text{ PgC yr}^{-1}$  when applying  
26 variable prior error assumptions. Seasonally-averaged posterior NEE SD varies from  $\sim 10\%$  to  $\sim 50\%$  of the multi-model-mean for  
27 different TransCom-3 land regions with significant NEE fluxes. On a global average, seasonal-average SD values range from  
28  $\sim 15\%$  (JJA) to  $\sim 30\%$  (DJF) of the posterior NEE mean. Note that these posterior NEE SD/range values here are similar to the  
29 baseline OSSEs conducted by changing prior NEE flux magnitudes (see Fig. 3). However, when comparing Fig. 4 and 3 (and Fig.  
30 S9), it is noticed that posterior NEE estimates are more sensitive to prior error assumptions compared to prior flux values in some  
31 seasons/regions of TL and SL (e.g., Northern Africa, Southern Africa, South America Temperate). It appears that NEE estimates  
32 during this study are more sensitive to prior error assumptions when sufficient observations are available and large differences  
33 between the prior and “truth” are present. Also, from Fig. 4 it can be seen that prior uncertainty assumptions in the baseline runs  
34 (using SD of prior models) and the assumption of 100% prior uncertainty tend to reproduce the “truth” more accurately than NEE  
35 estimates using 10% prior error. Overall, the results demonstrate that the posterior NEE fluxes over TransCom-3 land regions are  
36 in general similarly sensitive (up to  $\sim 50\%$ ) to the specification of prior flux uncertainties and the choice of bottom-up prior  
37 biospheric NEE model estimates.



### 1 3.6 OCO-2 ocean data

2 This portion of the study investigates the impact of assimilating OCO-2 OG XCO<sub>2</sub> data on posterior NEE flux estimates in our  
3 OSSE framework. To do this, four additional OSSE simulations were conducted with the four prior model NEEs when only  
4 assimilating synthetic OG retrievals (instead of LN+LG) in the inversions (everything else remains the same as in the baseline  
5 simulations). Figure 5 shows the results of these four additional OSSE simulations averaged over the TransCom-3 land regions.  
6 From these simulations it can be seen that OCO-2 OG indeed reduces the range in posterior NEE flux estimates, when applying  
7 different priors, compared to prior model predictions, and can generally reproduce the “truth”. On average, the spread in posterior  
8 NEE fluxes is ~20% to ~50% of the multi-model-mean for different TransCom-3 land regions with significant NEE fluxes. As  
9 expected, the comparison of Fig. 3 and 5 suggests that LN+LG data is better able to constrain biospheric CO<sub>2</sub> fluxes compared to  
10 OG data, as the spread among the posteriors is generally lower in LN+LG only assimilations (~70% lower on a global average)  
11 compared to OG data only assimilations. However, there were some cases where OSSE simulations using OCO-2 OG data alone  
12 did in fact result in slightly lower posterior NEE spreads in some TransCom-3 land regions compared to LN+LG assimilations  
13 runs (e.g., Northern Boreal regions during summer months and Australia during winter months). Overall, our OSSE simulations  
14 using the OCO-2 OG data demonstrate the importance of these oceanic retrievals to constrain land NEE fluxes, as the posterior  
15 NEE range is much lower compared to prior NEE estimates (see Fig. 5). This generally agrees with previous studies that  
16 demonstrated the importance of satellite data over the ocean in constraining NEE fluxes over land regions (e.g., Deng et al., 2016).

### 17 4. Conclusions

18 To the best of our understanding, this is the first study directly quantifying the impact of different prior global land biosphere  
19 models on the estimate of terrestrial CO<sub>2</sub> fluxes when assimilating OCO-2 satellite observations. We conducted a series of OSSEs  
20 that assimilated synthetic OCO-2 observations applying four state-of-the-science biospheric CO<sub>2</sub> flux models as the prior  
21 information. These controlled experiments were designed to systematically assess the impact of prior NEE fluxes and the impact  
22 of prior error assumptions on “top down” NEE estimates using OCO-2 data. The OSSEs incorporated NEE fluxes from the NASA-  
23 CASA, CASA-GFED, SiB-4 and LPJ biosphere models as prior estimates and variable prior flux error assumptions.

24 We found that the assimilation of synthetic OCO-2 XCO<sub>2</sub> retrievals resulted in posterior monthly/seasonal NEE estimates  
25 that generally reproduced the assumed “true” NEE globally and regionally. However, spread in posterior NEE exists in regions  
26 during seasons with poor data coverage, such as the Northern Boreal regions and some of the Tropical and Southern Hemispheric  
27 regions (e.g., South American Temperate, South Africa, Tropical Asia). This spread among posterior NEEs is likely due to the  
28 insufficient OCO-2 observations during winter over Northern Boreal regions and the large range among the priors in some of the  
29 Northern Boreal, Tropical and Southern Hemispheric regions. Residual spread from ~10% to 50% in seasonally-averaged posterior  
30 NEEs in TransCom-3 land regions with significant NEE flux were calculated due to using different prior models in inverse model  
31 simulations. We also found similar spreads in the magnitudes of posterior NEEs by conducting additional OSSEs using a single  
32 prior NEE flux model with variable prior flux uncertainty assumptions. While the spread in posterior NEE estimates, when using  
33 variable prior error statistics, was similar to when applying variable NEE flux models, the impact was larger in some seasons in  
34 the TL and SL regions. We determined that while OCO-2 observations on average constrain global, hemispheric and regional  
35 biospheric fluxes, noticeable residual differences (up to ~20-30% globally and 50% regionally) in posterior NEE flux estimates  
36 remain that were caused by the choice of prior model values and the specification of prior flux uncertainties.

37 There have been previous studies that investigated similar scientific objectives, such as the impact of prior uncertainties  
38 on inverse model estimates of NEE (Gurney et al., 2003; Chevalier et al., 2005; Baker et al., 2006a; 2010). The sensitivity of CO<sub>2</sub>  
39 flux inversions to the specification of prior flux information was first assessed by Gurney et al. (2003) using ground-based in situ



1 data. One main conclusion from Gurney et al. (2003) is that CO<sub>2</sub> flux estimates were sensitive to the prior flux uncertainty over  
2 regions with limited observations and insensitive over data-rich regions. Chevallier et al. (2005) suggested the importance of an  
3 accurate formulation of prior flux uncertainty by conducting 4D-Var assimilation of satellite column retrievals of CO<sub>2</sub>. Baker et  
4 al. (2010) investigated the importance of assumed prior flux uncertainties by conducting sensitivity tests that mistuned the  
5 assimilations by using incorrect prior flux errors. Finally, Baker et al. (2006a, 2010) suggested the need for realistic prior models  
6 in the 4D-Var assimilations using OCO synthetic satellite CO<sub>2</sub> data. The results of this research are generally consistent with the  
7 findings of these past studies. However, in comparison with these previous efforts, our study is a step forward, because we quantify  
8 the specific impact of prior model NEE spatio-temporal magnitude and prior uncertainties in optimizing regional and seasonal  
9 NEEs using satellite data in a more controlled manner by applying an OSSE framework.

10 The results of this study suggest the need to be aware of the residual impact from prior assumptions for CO<sub>2</sub> global flux  
11 inversions, especially for regions and times 1) where current “bottom-up” biosphere models diverge greatly and 2) without  
12 sufficient observational coverage from space-borne platforms. For example, larger spread in posterior NEE estimates were  
13 calculated in portions of the Northern Boreal regions that tend to have insufficient satellite data coverage and moderate differences  
14 among prior biosphere models. In addition to these Northern Boreal regions, Tropical and Southern Hemispheric regions with  
15 large spread among prior biosphere models, which are assigned higher prior uncertainty values resulting in largely reduced spreads  
16 in posterior NEE estimates (large deviation from the prior), still have residual impact from the prior NEE predictions regardless of  
17 the fact that OCO-2 data is dense in these regions. Results of this study also indicate that in some regions/seasons of the TL and  
18 SL, inverse model estimates of NEE can be more sensitive to prior error statistics compared to prior flux values. Overall, in data-  
19 poor regions/times, posterior estimates from inversion techniques relying on Bayesian statistics can result in similar estimates to  
20 the prior flux, however, with some improvements over broader regions. Additionally, in regions/seasons where uncertainty in NEE  
21 fluxes are large (e.g., in the TL where prior model NEE differences are large), inverse model estimates, applying large prior  
22 uncertainty values, will still have some residual impact from the choice of prior NEE flux. Finally, care should be given when  
23 interpreting flux estimates constrained with real OCO-2 satellite data over some of the regions identified in this study as it is  
24 suggested here that residual differences (up to ~20-30% globally and 50% regionally) in posterior NEE flux estimates can be  
25 produced by the choice of prior model values and the specification of prior flux uncertainties. In the future, studies should be  
26 designed to determine the relative importance of prior flux magnitudes and error assumptions on posterior estimates, in comparison  
27 with other error sources in inverse flux estimates (such as transport model errors and observation errors). Finally, the results of this  
28 study suggest that multi-inverse model inter-comparison studies should consider the differences in posterior NEE flux estimates  
29 caused by variable prior fluxes and error statistics used in different models.

### 30 **5. Code and Data Availability**

31 The forward and inverse model simulations for this work were performed using the GEOS-Chem model which is publicly available  
32 at: <http://acmg.seas.harvard.edu/geos/>. The 10-sec OCO-2 data used to produce synthetic observations during this study are  
33 available by request from the OCO-2 Science Team and individual OCO-2 sounding data can be downloaded here:  
34 <https://oco.jpl.nasa.gov/>.

### 35 **6. Author Contributions**

36 SP and MJ designed the methods and experiments presented in the study and analyzed results. CP, VG, DB, KH and BP were  
37 instrumental in providing biosphere model and OCO-2 data and guidance when applying these products. DH, JL and DB provided



1 components implemented in the modeling framework applied during this study. Finally, SP prepared the manuscript with  
2 contributions from all listed coauthors.

### 3 Acknowledgements

4 Sajeev Philip's research was supported by an appointment to the NASA Postdoctoral Program at the NASA Ames Research Center,  
5 administered by Universities Space Research Association under contract with NASA. DKH recognizes support from  
6 NA14OAR4310136. Resources supporting this work were provided by the NASA High-End Computing Program through the  
7 NASA Advanced Supercomputing Division at NASA Ames Research Center. We thank the OCO-2 Science Team for providing  
8 the version 8 OCO-2 product. We also thank the OCO-2 Flux Inversion Team, GEOS-Chem model developers, CASA-GFED  
9 team and NASA Carbon Monitoring System program for the free availability of their products. CarbonTracker CT2016 prior and  
10 posterior ocean fluxes were provided by National Oceanographic and Atmospheric Administration's Earth System Research  
11 Laboratory, Boulder, Colorado, USA from the website at <http://carbontracker.noaa.gov>. We are thankful to Sourish Basu, Feng  
12 Deng, Ray Nassar and Tom Oda for sharing data. We thank the support from the Earth Science Division of NASA Ames Research  
13 Center. The views, opinions and findings contained in this report are those of the authors and should not be construed as an official  
14 NASA or United States Government position, policy, or decision.

### 15 References

- 16 Baker, D. F., Doney, S. C., and Schimel, D. S.: Variational data assimilation for atmospheric CO<sub>2</sub>, *Tellus B*, 58, 359–365,  
17 <https://doi.org/10.1111/j.1600-0889.2006.00218.x>, 2006a.
- 18 Baker, D. F., Law, R. M., Gurney, K. R., Rayner, P., Peylin, P., Denning, A. S., Bousquet, P., Bruhwiler, L., Chen, Y. H., Ciais,  
19 P., Fung, I. Y., Heimann, M., John, J., Maki, T., Maksyutov, S., Masarie, K., Prather, M., Pak, B., Taguchi, S., and Zhu, Z.:  
20 TransCom 3 inversion intercomparison: Impact of transport model errors on the interannual variability of regional CO<sub>2</sub> fluxes,  
21 1988–2003, *Global Biogeochem. Cy.*, 20, GB1002, <https://doi.org/10.1029/2004gb002439>, 2006b.
- 22 Baker, D. F., Bösch, H., Doney, S. C., O'Brien, D., and Schimel, D. S.: Carbon source/sink information provided by column CO<sub>2</sub>  
23 measurements from the Orbiting Carbon Observatory, *Atmos. Chem. Phys.*, 10, 4145–4165, [https://doi.org/10.5194/acp-10-](https://doi.org/10.5194/acp-10-4145-2010)  
24 4145-2010, 2010.
- 25 Baker, I. T., Harper, A. B., da Rocha, H. R., Denning, A. S., Araújo, A. C., Borma, L. S., Freitas, H. C., Goulden, M. L., Manzi,  
26 A. O., Miller, S. D., Nobre, A. D., Restrepo-Coupe, N., Saleska, S. R., Stöckli, R., von Randow, C., and Wofsy, S. C.: Surface  
27 ecophysiological behavior across vegetation and moisture gradients in tropical South America, *Agric. For. Meteorol.*, 182–  
28 183, 177–188, <https://doi.org/10.1016/j.agrformet.2012.11.015>, 2013.
- 29 Basu, S., Guerlet, S., Butz, A., Houweling, S., Hasekamp, O., Aben, I., Krummel, P., Steele, P., Langenfelds, R., Torn, M., Biraud,  
30 S., Stephens, B., Andrews, A., and Worthy, D.: Global CO<sub>2</sub> fluxes estimated from GOSAT retrievals of total column CO<sub>2</sub>,  
31 *Atmos. Chem. Phys.*, 13, 8695–8717, <https://doi.org/10.5194/acp-13-8695-2013>, 2013.
- 32 Basu, S., Baker, D. F., Chevallier, F., Patra, P. K., Liu, J., and Miller, J. B.: The impact of transport model differences on CO<sub>2</sub>  
33 surface flux estimates from OCO-2 retrievals of column average CO<sub>2</sub>, *Atmos. Chem. Phys.*, 18, 7189–7215,  
34 <https://doi.org/10.5194/acp-18-7189-2018>, 2018.



- 1 Bey, I., Jacob, D. J., Yantosca, R. M., Logan, J. A., Field, B. D., Fiore, A. M., Li, Q. B., Liu, H. G. Y., Mickley, L. J., and Schultz,  
2 M. G.: Global modeling of tropospheric chemistry with assimilated meteorology: Model description and evaluation, *J.*  
3 *Geophys. Res. Atmos.*, 106, 23073–23095, <https://doi.org/10.1029/2001JD000807>, 2001.
- 4 Bowman, K. W.: Carbon Monitoring System Flux for Shipping, Aviation, and Chemical Sources L4 V1, Greenbelt, MD, USA,  
5 Goddard Earth Sciences Data and Information Services Center (GES DISC), Accessed [February 19, 2018],  
6 <https://doi.org/10.5067/RLT7JTCRJ11M>, 2017.
- 7 Bowman, K. W., Liu, J., Bloom, A. A., Parazoo, N. C., Lee, M., Jiang, Z., Menemenlis, D., Gierach, M. M., Collatz, G. J., Gurney,  
8 K. R., and Wunch D.: Global and Brazilian carbon response to El Niño Modoki 2011–2010, *Earth and Space Sci.*, 4, 637–  
9 660, <https://doi.org/10.1002/2016EA000204>, 2017.
- 10 Byrne, B., Jones, D. B. A., Strong, K., Zeng, Z.-C., Deng, F., and Liu, J.: Sensitivity of CO<sub>2</sub> surface flux constraints to observational  
11 coverage, *J. Geophys. Res. Atmos.*, 122, 6672–6694, <https://doi.org/10.1002/2016JD026164>, 2017.
- 12 Chevallier, F., Fisher, M., Peylin, P., Serrar, S., Bousquet, P., Bréon, F.-M., Chédin, A., and Ciais, P.: Inferring CO<sub>2</sub> sources and  
13 sinks from satellite observations: Method and application to TOVS data, *J. Geophys. Res. Atmos.*, 110, D24309,  
14 <https://doi.org/10.1029/2005JD006390>, 2005.
- 15 Chevallier, F., Feng, L., Bösch, H., Palmer, P. I., and Rayner, P. J.: On the impact of transport model errors for the estimation of  
16 CO<sub>2</sub> surface fluxes from GOSAT observations, *Geophys. Res. Lett.*, 37, L21803, <https://doi.org/10.1029/2010GL044652>,  
17 2010.
- 18 Chevallier, F., Palmer, P. I., Feng, L., Bösch, H., O'Dell, C. W., and Bousquet, P.: Toward robust and consistent regional CO<sub>2</sub>  
19 flux estimates from in situ and spaceborne measurements of atmospheric CO<sub>2</sub>, *Geophys. Res. Lett.*, 41, 1065–1070,  
20 <https://doi.org/10.1002/2013GL058772>, 2014.
- 21 Corbett, J. J. and Koehler, H. W.: Updated emissions from ocean shipping, *J. Geophys. Res. Atmos.*, 108(D20), 4650,  
22 <https://doi.org/10.1029/2003JD003751>, 2003.
- 23 Corbett, J. J. and Koehler, H. W.: Considering alternative input parameters in an activity-based ship fuel consumption and  
24 emissions model: Reply to comment by Øyvind Endresen et al. on “Updated emissions from ocean shipping”, *J. Geophys.*  
25 *Res. Atmos.*, 109, D23303, <https://doi.org/10.1029/2004JD005030>, 2004.
- 26 Crisp, D., Pollock, H. R., Rosenberg, R., Chapsky, L., Lee, R. A. M., Oyafuso, F. A., Frankenberg, C., O'Dell, C. W., Bruegge, C.  
27 J., Doran, G. B., Eldering, A., Fisher, B. M., Fu, D., Gunson, M. R., Mandrake, L., Osterman, G. B., Schwandner, F. M., Sun,  
28 K., Taylor, T. E., Wennberg, P. O., and Wunch, D.: The on-orbit performance of the Orbiting Carbon Observatory-2 (OCO-  
29 2) instrument and its radiometrically calibrated products, *Atmos. Meas. Tech.*, 10, 59–81, [https://doi.org/10.5194/amt-10-59-](https://doi.org/10.5194/amt-10-59-2017)  
30 2017, 2017.
- 31 Crowell, S. et al.: The 2015–2016 carbon cycle as seen from OCO-2 and the global in situ network, in preparation.
- 32 Deng, F., Jones, D. B. A., Henze, D. K., Bousserez, N., Bowman, K. W., Fisher, J. B., Nassar, R., O'Dell, C., Wunch, D., Wennberg,  
33 P. O., Kort, E. A., Wofsy, S. C., Blumenstock, T., Deutscher, N. M., Griffith, D. W. T., Hase, F., Heikkinen, P., Sherlock, V.,  
34 Strong, K., Sussmann, R., and Warneke, T.: Inferring regional sources and sinks of atmospheric CO<sub>2</sub> from GOSAT XCO<sub>2</sub>  
35 data, *Atmos. Chem. Phys.*, 14, 3703–3727, <https://doi.org/10.5194/acp-14-3703-2014>, 2014.
- 36 Deng, F., Jones, D. B. A., O'Dell, C. W., Nassar, R., and Parazoo, N. C.: Combining GOSAT XCO<sub>2</sub> observations over land and  
37 ocean to improve regional CO<sub>2</sub> flux estimates, *J. Geophys. Res. Atmos.*, 121, 1896–1913,  
38 <https://doi.org/10.1002/2015JD024157>, 2016.



- 1 Denning, A. S., Collatz, G. J., Zhang, C., Randall, D. A., Berry, J. A., Sellers, P. J., Colello, G. D., and Dazlich, D. A.: Simulations  
2 of terrestrial carbon metabolism and atmospheric CO<sub>2</sub> in a general circulation model, *Tellus B*, 48B, 521-542,  
3 <https://doi.org/10.1034/j.1600-0889.1996.t01-2-00009.x>, 1996.
- 4 Eldering, A., O'Dell, C. W., Wennberg, P. O., Crisp, D., Gunson, M. R., Viatte, C., Avis, C., Braverman, A., Castano, R., Chang,  
5 A., Chapsky, L., Cheng, C., Connor, B., Dang, L., Doran, G., Fisher, B., Frankenberg, C., Fu, D., Granat, R., Hobbs, J., Lee,  
6 R. A. M., Mandrake, L., McDuffie, J., Miller, C. E., Myers, V., Natraj, V., O'Brien, D., Osterman, G. B., Oyafuso, F., Payne,  
7 V. H., Pollock, H. R., Polonsky, I., Roehl, C. M., Rosenberg, R., Schwandner, F., Smyth, M., Tang, V., Taylor, T. E., To, C.,  
8 Wunch, D., and Yoshimizu, J.: The Orbiting Carbon Observatory-2: first 18 months of science data products, *Atmos. Meas.*  
9 *Tech.*, 10, 549-563, <https://doi.org/10.5194/amt-10-549-2017>, 2017a.
- 10 Eldering, A., Wennberg, P. O., Crisp, D., Schimel, D. S., Gunson, M. R., Chatterjee, A., Liu, J., Schwandner, F. M., Sun, Y.,  
11 O'Dell, C. W., Frankenberg, C., Taylor, T., Fisher, B., Osterman, G. B., Wunch, D., Hakkarainen, J., Tamminen, J., and Weir,  
12 B.: The Orbiting Carbon Observatory-2 early science investigations of regional carbon dioxide fluxes, *Science*,  
13 358, eaam5745, <https://doi.org/10.1126/science.aam5745>, 2017b.
- 14 Fisher, J. B., Sikka, M., Huntzinger, D. N., Schwalm, C., and Liu, J.: Technical note: 3-hourly temporal downscaling of monthly  
15 global terrestrial biosphere model net ecosystem exchange, *Biogeosciences*, 13, 4271-4277, [https://doi.org/10.5194/bg-13-](https://doi.org/10.5194/bg-13-4271-2016)  
16 4271-2016, 2016a.
- 17 Fisher, J. B., Sikka, M., Huntzinger, D. N., Schwalm, C. R., Liu, J., Wei, Y., Cook, R. B., Michalak, A. M., Schaefer, K., Jacobson,  
18 A. R., Arain, M. A., Ciais, P., El-masri, B., Hayes, D. J., Huang, M., Huang, S., Ito, A., Jain, A. K., Lei, H., Lu, C., Maignan,  
19 F., Mao, J., Parazoo, N. C., Peng, C., Peng, S., Poulter, B., Ricciuto, D. M., Tian, H., Shi, X., Wang, W., Zeng, N., Zhao, F.,  
20 and Zhu, Q.: CMS: Modeled Net Ecosystem Exchange at 3-hourly Time Steps, 2004-2010, ORNL DAAC, Oak Ridge,  
21 Tennessee, USA., <https://doi.org/10.3334/ORNLDAAC/1315>, 2016b.
- 22 Gurney, K. R., Law, R. M., Denning, A. S., Rayner, P. J., Baker, D., Bousquet, P., Bruhwiler, L., Chen, Y.-H., Ciais, P., Fan, S.,  
23 Fung, I. Y., Gloor, M., Heimann, M., Higuchi, K., John, J., Kowalczyk, E., Maki, T., Maksyutov, S., Peylin, P., Prather, M.,  
24 Pak, B. C., Sarmiento, J., Taguchi, S., Takahashi, T., and Yuen, C.-W.: TransCom 3 CO<sub>2</sub> inversion intercomparison: 1. Annual  
25 mean control results and sensitivity to transport and prior flux information, *Tellus B*, 55B, 555-579,  
26 <https://doi.org/10.1034/j.1600-0889.2003.00049.x>, 2003.
- 27 Harris, I., Jones, P. D., Osborn, T. J., and Lister, D. H.: Updated high-resolution grids of monthly climatic observations – the CRU  
28 TS3.10 Dataset, *Int. J. Climatol.*, 34, 623-642, <https://doi.org/10.1002/joc.3711>, 2013.
- 29 Haxeltine, A., and Prentice, I. C.: A general model for the light-use efficiency of primary production. *Funct. Ecol.*, 10, 551-561,  
30 <https://doi.org/10.2307/2390165>, 1996.
- 31 Haynes, K. D., Baker, I. T., Denning, A. S., Stöckli, R., Schaefer, K., and Lokupitiya, E.: Global Self-Consistent Carbon Flux and  
32 Pool Estimates Utilizing the Simple Biosphere Model (SiB4). Abstract B31F-01 presented at 2013 AGU Fall Meeting, AGU,  
33 San Francisco, CA, 9-13 December, 2013.
- 34 Heimann, M., Esser, G., Haxeltine, A., Kaduk, J., Kicklighter, D. W., Knorr, W., Kohlmaier, G. H., McGuire, A. D., Melillo, J.,  
35 Moore III, B., Otto, R. D., Prentice, I. C., Sauf, W., Schloss, A., Sitch, S., Wittenberg, U., and Würth, G.: Evaluation of  
36 terrestrial Carbon Cycle models through simulations of the seasonal cycle of atmospheric CO<sub>2</sub>: First results of a model  
37 intercomparison study, *Global Biogeochem. Cy.*, 12, 1–24, <https://doi.org/10.1029/97GB01936>, 1998.



- 1 Henze, D. K., Hakami, A., and Seinfeld, J. H.: Development of the adjoint of GEOS-Chem, *Atmos. Chem. Phys.*, 7, 2413-2433,  
2 <https://doi.org/10.5194/acp-7-2413-2007>, 2007.
- 3 Houweling, S., Aben, I., Breon, F.-M., Chevallier, F., Deutscher, N., Engelen, R., Gerbig, C., Griffith, D., Hungershofer, K.,  
4 Macatangay, R., Marshall, J., Notholt, J., Peters, W., and Serrar, S.: The importance of transport model uncertainties for the  
5 estimation of CO<sub>2</sub> sources and sinks using satellite measurements, *Atmos. Chem. Phys.*, 10, 9981-9992,  
6 <https://doi.org/10.5194/acp-10-9981-2010>, 2010.
- 7 Houweling, S., Baker, D., Basu, S., Boesch, H., Butz, A., Chevallier, F., Deng, F., Dlugokencky, E. J., Feng, L., Ganshin, A.,  
8 Hasekamp, O., Jones, D., Maksyutov, S., Marshall, J., Oda, T., O'Dell, C. W., Oshchepkov, S., Palmer, P. I., Peylin, P., Poussi,  
9 Z., Reum, F., Takagi, H., Yoshida, Y., and Zhuravlev, R.: An intercomparison of inverse models for estimating sources and  
10 sinks of CO<sub>2</sub> using GOSAT measurements, *J. Geophys. Res. Atmos.*, 120, 5253–5266, <https://doi.org/10.1002/2014JD022962>,  
11 2015.
- 12 Huntzinger, D. N., Post, W. M., Wei, Y., Michalak, A. M., West T. O., Jacobson, A. R., Baker, I. T., Chen, J. M., Davis, K. J.,  
13 Hayes, D. J., Hoffman, F. M., Jain, A. K., Liu, S., McGuire, A. D., Neilson, R. P., Potter, C., Poulter, B., Price, D., Raczka,  
14 B. M., Tian, H., Q., Thornton, P., Tomelleri, E., Viovy, N., Xiao, J., Yuan, W., Zeng, N., Zhao, M., and Cook, R.: North  
15 American Carbon Program (NACP) regional interim synthesis: Terrestrial biospheric model intercomparison, *Ecol. Model.*,  
16 232, 144-157, <https://doi.org/10.1016/j.ecolmodel.2012.02.004>, 2012.
- 17 Huntzinger, D. N., Schwalm, C., Michalak, A. M., Schaefer, K., King, A. W., Wei, Y., Jacobson, A., Liu, S., Cook, R. B., Post,  
18 W. M., Berthier, G., Hayes, D., Huang, M., Ito, A., Lei, H., Lu, C., Mao, J., Peng, C. H., Peng, S., Poulter, B., Ricciuto, D.,  
19 Shi, X., Tian, H., Wang, W., Zeng, N., Zhao, F., and Zhu, Q.: The North American Carbon Program Multi-Scale Synthesis  
20 and Terrestrial Model Intercomparison Project – Part 1: Overview and experimental design, *Geosci. Model Dev.*, 6, 2121-  
21 2133, <https://doi.org/10.5194/gmd-6-2121-2013>, 2013.
- 22 Huntzinger, D. N., Schwalm, C. R., Wei, Y., Cook, R. B., Michalak, A. M., Schaefer, K., Jacobson, A. R., Arain, M. A., Ciais, P.,  
23 Fisher, J. B., Hayes, D. J., Huang, M., Huang, S., Ito, A., Jain, A. K., Lei, H., Lu, C., Maignan, F., Mao, J., Parazoo, N. C.,  
24 Peng, C., Peng, S., Poulter, B., Ricciuto, D. M., Tian, H., Shi, X., Wang, W., Zeng, N., Zhao, F., Zhu, Q., Yang, J., and Tao,  
25 B.: NACP MstMIP: Global 0.5-degree Model Outputs in Standard Format, Version 1.0. ORNL DAAC, Oak Ridge,  
26 Tennessee, USA. <https://doi.org/10.3334/ORNLDAAC/1225>, 2018.
- 27 IPCC, 2014: Climate Change 2014: Synthesis Report. Contribution of Working Groups I, II and III to the Fifth Assessment Report  
28 of the Intergovernmental Panel on Climate Change [Core Writing Team, R.K. Pachauri and L.A. Meyer (eds.)], IPCC, Geneva,  
29 Switzerland, 151 pp, 2014.
- 30 Ito, A., Inatomi, M., Huntzinger, D. N., Schwalm, C., Michalak, A. M., Cook, R., King, A. W., Mao, J., Wei, Y., Post, W. M.,  
31 Wang, W., Arain, M. A., Huang, S., Hayes, D. J., Ricciuto, D. M., Shi, X., Huang, M., Lei, H., Tian, H., Lu, C., Yang, J., Tao,  
32 B., Jain, A., Poulter, B., Peng, S., Ciais, P., Fisher, J. B., Parazoo, N. C., Schaefer, K., Peng, C., Zeng, N., and Zhao, F.:  
33 Decadal trends in the seasonal-cycle amplitude of terrestrial CO<sub>2</sub> exchange resulting from the ensemble of terrestrial biosphere  
34 models, *Tellus B*, 68, 28968, <https://doi.org/10.3402/tellusb.v68.28968>, 2016.
- 35 Landschützer, P., Gruber, N., and Bakker, D. C. E.: Decadal variations and trends of the global ocean carbon sink, *Global*  
36 *Biogeochem. Cy.*, 30, 1396–1417, <https://doi.org/10.1002/2015GB005359>, 2016.
- 37 Landschützer, P., Gruber, N., and Bakker, D. C. E.: An updated observation-based global monthly gridded sea surface pCO<sub>2</sub> and  
38 air-sea CO<sub>2</sub> flux product from 1982 through 2015 and its monthly climatology (NCEI Accession 0160558), Version 2.2,  
39 NOAA National Centers for Environmental Information, Dataset, [2017-07-11], 2017.



- 1 Law, R. M., Chen, Y-H., Gurney, K. R., and TransCom 3 modelers: TransCom 3 CO<sub>2</sub> inversion intercomparison: 2. Sensitivity of  
2 annual mean results to data choices, *Tellus B*, 55B, 580-595, <https://doi.org/10.1034/j.1600-0889.2003.00053.x>, 2003.
- 3 Le Quéré, C., Andrew, R. M., Friedlingstein, P., Sitch, S., Pongratz, J., Manning, A. C., Korsbakken, J. I., Peters, G. P., Canadell,  
4 J. G., Jackson, R. B., Boden, T. A., Tans, P. P., Andrews, O. D., Arora, V. K., Bakker, D. C. E., Barbero, L., Becker, M.,  
5 Betts, R. A., Bopp, L., Chevallier, F., Chini, L. P., Ciais, P., Cosca, C. E., Cross, J., Currie, K., Gasser, T., Harris, I., Hauck,  
6 J., Haverd, V., Houghton, R. A., Hunt, C. W., Hurtt, G., Ilyina, T., Jain, A. K., Kato, E., Kautz, M., Keeling, R. F., Klein  
7 Goldewijk, K., Körtzinger, A., Landschützer, P., Lefèvre, N., Lenton, A., Lienert, S., Lima, I., Lombardozzi, D., Metzl, N.,  
8 Millero, F., Monteiro, P. M. S., Munro, D. R., Nabel, J. E. M. S., Nakaoka, S.-I., Nojiri, Y., Padin, X. A., Peregón, A., Pfeil,  
9 B., Pierrot, D., Poulter, B., Rehder, G., Reimer, J., Rödenbeck, C., Schwinger, J., Séférian, R., Skjelvan, I., Stocker, B. D.,  
10 Tian, H., Tilbrook, B., Tubiello, F. N., van der Laan-Luijkx, I. T., van der Werf, G. R., van Heuven, S., Viovy, N., Vuichard,  
11 N., Walker, A. P., Watson, A. J., Wiltshire, A. J., Zaehle, S., and Zhu, D.: Global Carbon Budget 2017, *Earth Syst. Sci. Data*,  
12 10, 405-448, <https://doi.org/10.5194/essd-10-405-2018>, 2018.
- 13 Liu, D. C., and Nocedal J.: On the limited memory BFGS method for large scale optimization, *Math. Prog.*, 45, 503-528,  
14 <https://doi.org/10.1007/bf01589116>, 1989.
- 15 Liu, J., Bowman, K. W., Lee, M., Henze, D. K., Bousserez, N., Brix, H., Collatz, G. J., Menemenlis, D., Ott, L., Pawson, S., Jones,  
16 D., and Ray Nassar, R.: Carbon monitoring system flux estimation and attribution: impact of ACOS-GOSAT XCO<sub>2</sub> sampling  
17 on the inference of terrestrial biospheric sources and sinks, *Tellus B*, 66, 22486, <https://doi.org/10.3402/tellusb.v66.22486>,  
18 2014.
- 19 Liu, J., Bowman, K. W., Schimel, D. S., Parazoo, N. C., Jiang, Z., Lee, M., Bloom, A. A., Wunch, D., Frankenberg, C., Sun, Y.,  
20 O'Dell, C. W., Gurney, K. R., Menemenlis, D., Gierach, M., Crisp, D., and Eldering A.: Contrasting carbon cycle responses  
21 of the tropical continents to the 2015–2016 El Niño, *Science*, 358, eaam5690, <https://doi.org/10.1126/science.aam5690>, 2017.
- 22 Lokupitiya, E., Denning, A. S., Paustian, K., Baker, I., Schaefer, K., Verma, S., Meyers, T., Bernacchi, C. J., Suyker, A., and  
23 Fischer, M.: Incorporation of crop phenology in Simple Biosphere Model (SiBcrop) to improve land-atmosphere carbon  
24 exchanges from croplands, *Biogeosciences*, 6, 969-986, <https://doi.org/10.5194/bg-6-969-2009>, 2009.
- 25 Nassar, R., Jones, D. B. A., Suntharalingam, P., Chen, J. M., Andres, R. J., Wecht, K. J., Yantosca, R. M., Kulawik, S. S., Bowman,  
26 K. W., Worden, J. R., Machida, T., and Matsueda, H.: Modeling global atmospheric CO<sub>2</sub> with improved emission inventories  
27 and CO<sub>2</sub> production from the oxidation of other carbon species, *Geosci. Model Dev.*, 3, 689-716, <https://doi.org/10.5194/gmd-3-689-2010>, 2010.
- 28
- 29 Nassar, R., Napier-Linton, L., Gurney, K. R., Andres, R. J., Oda, T., Vogel, F. R., and Deng, F.: Improving the temporal and spatial  
30 distribution of CO<sub>2</sub> emissions from global fossil fuel emission data sets, *J. Geophys. Res. Atmos.*, 118, 917-933,  
31 <https://doi.org/10.1029/2012JD018196>, 2013.
- 32 Oda, T., Maksyutov, S., and Andres, R. J.: The Open-source Data Inventory for Anthropogenic CO<sub>2</sub>, version 2016 (ODIAC2016):  
33 a global monthly fossil fuel CO<sub>2</sub> gridded emissions data product for tracer transport simulations and surface flux inversions,  
34 *Earth Syst. Sci. Data*, 10, 87-107, <https://doi.org/10.5194/essd-10-87-2018>, 2018.
- 35 O'Dell, C. W., Connor, B., Bösch, H., O'Brien, D., Frankenberg, C., Castano, R., Christi, M., Eldering, D., Fisher, B., Gunson, M.,  
36 McDuffie, J., Miller, C. E., Natraj, V., Oyafuso, F., Polonsky, I., Smyth, M., Taylor, T., Toon, G. C., Wennberg, P. O., and  
37 Wunch, D.: The ACOS CO<sub>2</sub> retrieval algorithm – Part 1: Description and validation against synthetic observations, *Atmos.*  
38 *Meas. Tech.*, 5, 99-121, <https://doi.org/10.5194/amt-5-99-2012>, 2012.



- 1 Olsen, S. C. and Randerson, J. T.: Differences between surface and column atmospheric CO<sub>2</sub> and implications for carbon cycle  
2 research, *J. Geophys. Res. Atmos.*, 109, D02301, <https://doi.org/10.1029/2003JD003968>, 2004.
- 3 Olsen, S. C., Wuebbles, D. J., and Owen, B.: Comparison of global 3-D aviation emissions datasets, *Atmos. Chem. Phys.*, 13, 429-  
4 441, <https://doi.org/10.5194/acp-13-429-2013>, 2013.
- 5 Ott, L. E., Pawson, S., Collatz, G. J., Gregg, W. W., Menemenlis, D., Brix, H., Rousseaux, C. S., Bowman, K. W., Liu, J., Eldering,  
6 A., Gunson, M. R., and Kawa, S. R.: Assessing the magnitude of CO<sub>2</sub> flux uncertainty in atmospheric CO<sub>2</sub> records using  
7 products from NASA's Carbon Monitoring Flux Pilot Project, *J. Geophys. Res. Atmos.*, 120, 734–765,  
8 <https://doi.org/10.1002/2014JD022411>, 2015.
- 9 Peng, S., Ciais, P., Chevallier, F., Peylin, P., Cadule, P., Sitch, S., Piao, S., Ahlström, A., Huntingford, C., Levy, P., Li, X., Liu,  
10 Y., Lomas, M., Poulter, B., Viogy, N., Wang, T., Wang, X., Zaehle, S., Zeng, N., Zhao, F., and Zhao, H.: Benchmarking the  
11 seasonal cycle of CO<sub>2</sub> fluxes simulated by terrestrial ecosystem models, *Global Biogeochem. Cy.*, 29, 46–64,  
12 <https://doi.org/10.1002/2014GB004931>, 2015.
- 13 Peylin, P., Law, R. M., Gurney, K. R., Chevallier, F., Jacobson, A. R., Maki, T., Niwa, Y., Patra, P. K., Peters, W., Rayner, P. J.,  
14 Rödenbeck, C., van der Laan-Luijckx, I. T., and Zhang, X.: Global atmospheric carbon budget: results from an ensemble of  
15 atmospheric CO<sub>2</sub> inversions, *Biogeosciences*, 10, 6699–6720, <https://doi.org/10.5194/bg-10-6699-2013>, 2013.
- 16 Peters, W., Jacobson, A. R., Sweeney, C., Andrews, A. E., Conway, T. J., Masarie, K., Miller, J. B., Bruhwiler, L. M. P., Pétron,  
17 G., Hirsch, A. I., Worthy, D. E. J., van der Werf, G. R., Randerson, J. T., Wennberg, P. O., Krol, M. C., and Tans, P. P.: An  
18 atmospheric perspective on North American carbon dioxide exchange: CarbonTracker, *Proc. Natl. Acad. Sci.*, 104, 18925–  
19 18930, <https://doi.org/10.1073/pnas.0708986104>, 2007.
- 20 Potter, C., Randerson, J. T., Field, C. B., Matson, P. A., Vitousek, P. M., Mooney, H. A., and Klooster, S. A.: Terrestrial ecosystem  
21 production: A process model based on global satellite and surface data, *Global Biogeochem. Cy.*, 7, 811–841,  
22 <https://doi.org/10.1029/93GB02725>, 1993.
- 23 Potter, C., Klooster, S., Myneni, R., Genovesi, V., Tan, P.-N., and Kumar, V.: Continental scale comparisons of terrestrial carbon  
24 sinks estimated from satellite data and ecosystem modeling 1982–98, *Glob. Planet. Chang.*, 39, 201–213,  
25 <https://doi.org/10.1016/j.gloplacha.2003.07.001>, 2003.
- 26 Potter, C., Kumar, V., Klooster, S., and Nemani, R.: Recent history of trends in vegetation greenness and large-scale ecosystem  
27 disturbances in Eurasia, *Tellus B*, 59, 260–272, <https://doi.org/10.1111/j.1600-0889.2006.00245.x>, 2007.
- 28 Potter, C., Klooster, S., Huete, A., Genovesi, V., Bustamante, M., Guimaraes Ferreira, L., R. C. de Oliveira Jr., and Zepp, R.:  
29 Terrestrial carbon sinks in the Brazilian Amazon and Cerrado region predicted from MODIS satellite data and ecosystem  
30 modeling, *Biogeosciences*, 6, 937–945, <https://doi.org/10.5194/bg-6-937-2009>, 2009.
- 31 Potter, C., Klooster, S., and Genovesi, V.: Net primary production of terrestrial ecosystems from 2000 to 2009, *Climatic Change*,  
32 115, 365–378, <http://dx.doi.org/10.1007/s10584-012-0460-2>, 2012a.
- 33 Potter, C., Klooster, S., Genovesi, V., Hiatt, C., Boriah, S., Kumar, V., Mithal, V., and Garg, A.: Terrestrial ecosystem carbon  
34 fluxes predicted from MODIS satellite data and large-scale disturbance modeling, *Int. J. Geosci.*, 3, 469–479,  
35 <http://dx.doi.org/10.4236/ijg.2012.33050>, 2012b.
- 36 Poulter, B., Frank, D., Ciais, P., Myneni, R. B., Andela, N., Bi, J., Broquet, G., Canadell, J. G., Chevallier, F., Liu, Y. Y., Running,  
37 S. W., Sitch, S., and van der Werf, G. R.: Contribution of semi-arid ecosystems to interannual variability of the global carbon  
38 cycle, *Nature*, 509, 600–603, <http://dx.doi.org/10.1038/nature13376>, 2014.



- 1 Randerson, J. T., Thompson, M. V., Malmstrom, C. M., Field, C. B., and Fung, I. Y.: Substrate limitations for heterotrophs:  
2 Implications for models that estimate the seasonal cycle of atmospheric CO<sub>2</sub>, *Global Biogeochem. Cy.*, 10,, 585–602,  
3 <https://doi.org/10.1029/96GB01981>, 1996.
- 4 Rödenbeck, C., Houweling, S., Gloor, M., and Heimann, M.: CO<sub>2</sub> flux history 1982–2001 inferred from atmospheric data using a  
5 global inversion of atmospheric transport, *Atmos. Chem. Phys.*, 3, 1919–1964, <https://doi.org/10.5194/acp-3-1919-2003>, 2003.
- 6 Rödenbeck, C., Conway, T. J., and Langenfelds, R. L.: The effect of systematic measurement errors on atmospheric CO<sub>2</sub>  
7 inversions: a quantitative assessment, *Atmos. Chem. Phys.*, 6, 149–161, <https://doi.org/10.5194/acp-6-149-2006>, 2006.
- 8 Schaefer, K., Collatz, G. J., Tans, P., Denning, A. S., Baker, I., Berry, J., Prihodko, L., Suits, N., and Philpott, A.: Combined  
9 Simple Biosphere/Carnegie-Ames-Stanford Approach terrestrial carbon cycle model, *J. Geophys. Res. Biogeosci.*, 113,  
10 G03034, <https://doi.org/10.1029/2007JG000603>, 2008.
- 11 Schimel, D. S., House, J. I., Hibbard, K. A., Bousquet, P., Ciais, P., Peylin, P., Braswell, B. H., Apps, M. J., Baker, D., Bondeau,  
12 A., Canadell, J., Churkina, G., Cramer, W., Denning, A. S., Field, C. B., Friedlingstein, P., Goodale, C., Heimann, M.,  
13 Houghton, R. A., Melillo, J. M., Moore III, B., Murdiyarso, D., Noble, I., Pacala, S. W., Prentice, I. C., Raupach, M. R.,  
14 Rayner, P. J., Scholes, R. J., Steffen, W. L., and Wirth, C.: Recent patterns and mechanisms of carbon exchange by terrestrial  
15 ecosystems, *Nature*, 414, 169–172, <https://doi.org/10.1038/35102500>, 2001.
- 16 Schimel, D., Stephens, B. B., and Fisher, J. B.: Effect of increasing CO<sub>2</sub> on the terrestrial carbon cycle, *Proc. Natl. Acad. Sci.*, 112,  
17 436–441, <https://doi.org/10.1073/pnas.1407302112>, 2015.
- 18 Schwalm, C. R., Huntzinger, D. N., Fisher, J. B., Michalak, A. M., Bowman, K., Ciais, P., Cook, R., El-Masri, B., Hayes, D.,  
19 Huang, M., Ito, A., Jain, A., King, A. W., Lei, H., Liu, J., Lu, C., Mao, J., Peng, S., Poulter, B., Ricciuto, D., Schaefer, K.,  
20 Shi, X., Tao, B., Tian, H., Wang, W., Wei, Y., Yang, J., and Zeng, N.: Toward “optimal” integration of terrestrial biosphere  
21 models, *Geophys. Res. Lett.*, 42, 4418–4428, <https://doi.org/10.1002/2015GL064002>, 2015.
- 22 Seinfeld, J. H. and Pandis, S. N.: *Atmospheric chemistry and physics: from air pollution to climate change*, 3rd Edn. Wiley, 2016.
- 23 Sellers, P. J., Mintz, Y., Sud, Y. C., and Dalcher, A.: A simple biosphere model (SiB) for use within general circulation models, *J.*  
24 *Atmos. Sci.*, 43, 505–531, [https://doi.org/10.1175/1520-0469\(1986\)043<0505:ASBMFU>2.0.CO;2](https://doi.org/10.1175/1520-0469(1986)043<0505:ASBMFU>2.0.CO;2), 1986.
- 25 Sellers, P. J., Randall, D. A., Collatz, G. J., Berry, J. A., Field, C. B., Dazlich, D. A., Zhang, C., Collelo, G. D., and Buonoua, L.:  
26 A revised Land Surface Parameterization (SiB2) for atmospheric GCMs. Part I: Model formulation, *J. Clim.*, 9, 676–705,  
27 [https://doi.org/10.1175/1520-0442\(1996\)009<0676:ARLSPF>2.0.CO;2](https://doi.org/10.1175/1520-0442(1996)009<0676:ARLSPF>2.0.CO;2), 1996.
- 28 Sitch, S., Smith, B., Prentice, I. C., Arneth, A., Bondeau, A., Cramer, W., Kaplan, J. O., Levis, S., Lucht, W., Sykes, M. T.,  
29 Thonicke, K., and Venevsky, S.: Evaluation of ecosystem dynamics, plant geography and terrestrial carbon cycling in the LPJ  
30 dynamic global vegetation model, *Glob. Change Biol.*, 9, 161–185, <https://doi.org/10.1046/j.1365-2486.2003.00569.x>, 2003.
- 31 Suntharalingam, P., Jacob, D. J., Palmer, P. I., Logan, J. A., Yantosca, R. M., Xiao, Y., Evans, M. J., Streets, D. G., Vay, S. L.,  
32 and Sachse, G. W.: Improved quantification of Chinese carbon fluxes using CO<sub>2</sub>/CO correlations in Asian outflow, *J. Geophys.*  
33 *Res. Atmos.*, 109, D18S18, <https://doi.org/10.1029/2003JD004362>, 2004.
- 34 Sitch, S., Friedlingstein, P., Gruber, N., Jones, S. D., Murray-Tortarolo, G., Ahlström, A., Doney, S. C., Graven, H., Heinze, C.,  
35 Huntingford, C., Levis, S., Levy, P. E., Lomas, M., Poulter, B., Viovy, N., Zaehle, S., Zeng, N., Arneth, A., Bonan, G., Bopp,  
36 L., Canadell, J. G., Chevallier, F., Ciais, P., Ellis, R., Gloor, M., Peylin, P., Piao, S. L., Le Quéré, C., Smith, B., Zhu, Z., and  
37 Myneni, R.: Recent trends and drivers of regional sources and sinks of carbon dioxide, *Biogeosciences*, 12, 653–679,  
38 <https://doi.org/10.5194/bg-12-653-2015>, 2015.



- 1 Takagi H., Houweling, S., Andres, R. J., Belikov, D., Bril, A., Boesch H., Butz, A., Guerlet, S., Hasekamp, O., Maksyutov, S.,  
2 Morino, I., Oda T., O'Dell, C. W., Oshchepkov, S., Parker, R., Saito, M., Uchino, O., Yokota, T., Yoshida, Y., and Valsala,  
3 V.: Influence of differences in current GOSAT XCO<sub>2</sub> retrievals on surface flux estimation, *Geophys. Res. Lett.*, 41, 2598–  
4 2605, <https://doi.org/10.1002/2013GL059174>, 2014.
- 5 Takahashi, T., Sutherland, S. C., Wanninkhof, R., Sweeney, C., Feely, R. A., Chipman, D. W., Hales, B., Friederich, G., Chavez,  
6 F., Sabine, C., Watson, A., Bakker, D. C. E., Schuster, U., Metzl, N., Yoshikawa-Inoue, H., Ishii, M., Midorikawa, T., Nojiri,  
7 Y., Körtzinger, A., Steinhoff, T., Hoppema, M., Olafsson, J., Arnarson, T. S., Tilbrook, B., Johannessen, T., Olsen, A.,  
8 Bellerby, R., Wong, C. S., Delille, B., Bates, N. R., and de Baar, H. J. W.: Climatological mean and decadal change in surface  
9 ocean pCO<sub>2</sub>, and net sea-air CO<sub>2</sub> flux over the global oceans, *Deep Sea Res. II: Topical Stud. Oceanogr.*, 56, 554–577,  
10 <https://doi.org/10.1016/j.dsr2.2008.12.009>, 2009.
- 11 van der Werf, G. R., Randerson, J. T., Collatz, G. J., Giglio, L., Kasibhatla, P. S., Arellano, A. F., Olsen, S. C., and Kasischke, E.  
12 S.: Continental-scale partitioning of fire emissions during the 1997 to 2001 El Nino/La Nina period, *Science*, 303, 73–76,  
13 <https://doi.org/10.1126/science.1090753>, 2004.
- 14 van der Werf, G. R., Randerson, J. T., Giglio, L., Collatz, G. J., Kasibhatla, P. S., and Arellano Jr., A. F.: Interannual variability in  
15 global biomass burning emissions from 1997 to 2004, *Atmos. Chem. Phys.*, 6, 3423–3441, [https://doi.org/10.5194/acp-6-3423-](https://doi.org/10.5194/acp-6-3423-2006)  
16 2006, 2006.
- 17 van der Werf, G. R., Randerson, J. T., Giglio, L., Collatz, G. J., Mu, M., Kasibhatla, P. S., Morton, D. C., DeFries, R. S., Jin, Y.,  
18 and van Leeuwen, T. T.: Global fire emissions and the contribution of deforestation, savanna, forest, agricultural, and peat  
19 fires (1997–2009), *Atmos. Chem. Phys.*, 10, 11707–11735, <https://doi.org/10.5194/acp-10-11707-2010>, 2010.
- 20 Wang, J. S., Kawa, S. R., Collatz, G. J., Sasakawa, M., Gatti, L. V., Machida, T., Liu, Y., and Manyin, M. E.: A global synthesis  
21 inversion analysis of recent variability in CO<sub>2</sub> fluxes using GOSAT and in situ observations, *Atmos. Chem. Phys.*, 18, 11097–  
22 11124, <https://doi.org/10.5194/acp-18-11097-2018>, 2018.



1 **Table 1: Prior and (Posterior) global annual mean NEE fluxes and CO<sub>2</sub> emission inventories (PgC yr<sup>-1</sup>) for the year 2015 used in the**  
 2 **OSSE simulations during this study.**

NEE Model	NEE flux (PgC yr <sup>-1</sup> )
MsTMIP <sup>1,2</sup>	-4.31
NASA-CASA <sup>3</sup>	-1.86 (-4.14)
CASA-GFED <sup>4</sup>	-2.42 (-4.24)
SiB-4 <sup>5</sup>	0.95 (-4.11)
LPJ <sup>6</sup>	-5.53 (-4.36)
Inventory	CO <sub>2</sub> emission (PgC yr <sup>-1</sup> )
Fossil fuel <sup>7</sup>	9.86
Ocean <sup>8</sup>	-2.41
Biomass burning <sup>9</sup>	2.05
Fuel wood burning <sup>9</sup>	0.50

3 <sup>1</sup>MsTMIP NEE dataset is representative of the year 2010 and is an ensemble mean of 15 different NEE models.

4 <sup>2</sup>Huntzinger et al., 2013; 2016; Fisher et al., 2016a,2016b

5 <sup>3</sup>Potter et al., 1993; 2012a; 2012b

6 <sup>4</sup>Potter et al., 1993; Randerson et al., 1996

7 <sup>5</sup>Haynes et al., 2013; Baker et al., 2013

8 <sup>6</sup>Sitch et al., 2003; Poulter et al., 2014

9 <sup>7</sup>Oda et al., 2018; Nassar et al., 2013

10 <sup>8</sup>CarbonTracker CT2016; Peters et al., 2007

11 <sup>9</sup>CASA-GFED3; van der Werf et al., 2004; 2006; 2010

12



1 Table 2: Summary of the different OSSEs conducted during this work.

Experiment (# of OSSEs)	OCO-2 XCO <sub>2</sub> Mode	Prior NEE Model	NEE Uncertainty
Variable Prior NEE (4)	LN + LG	All <sup>1</sup>	Multi-Model SD <sup>2</sup>
Variable Prior NEE (4)	OG	All <sup>1</sup>	Multi-Model SD <sup>2</sup>
Variable Prior Uncert. (2)	LN + LG	CASA-GFED	Uniform 10%/100%

2 <sup>1</sup> NASA-CASA, CASA-GFED, SiB-4 and LPJ3 <sup>2</sup> SD = standard deviation

4

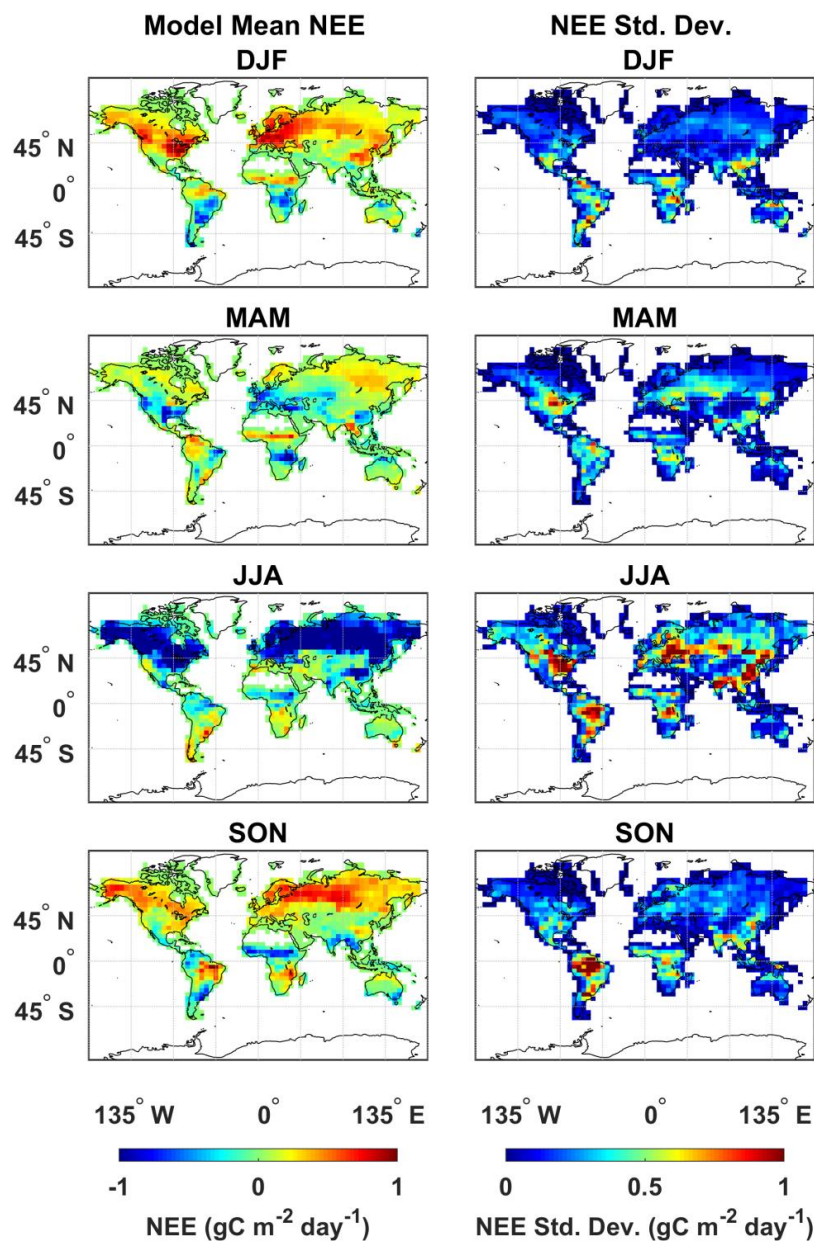


1 Table 3: Seasonally-averaged NEE ( $\text{PgC yr}^{-1}$ ) averaged over the 11 TransCom-3 land regions (refer to Fig. S2) for the MsTMIP (“truth”),  
 2 multi-model prior mean and multi-model posterior mean ( $\text{PgC yr}^{-1}$ ). The differences between the prior and posterior model NEE values  
 3 are presented as SD ( $1\sigma$ ) and range. Prior model values are presented in standard font and posterior estimates are in bold. Seasons are  
 4 represented as Winter (W): December-February, Spring (Sp): March-May, Summer (Su): June-August and Fall (F): September-  
 5 November.

Region*	NEE: Truth				NEE: Mean				NEE: Standard Deviation				NEE: Range															
	W	Sp	Su	F	W	Sp	Su	F	W	Sp	Su	F	W	Sp	Su	F												
1	1.1	-0.2	-2.8	0.7	1.1	<b>1.0</b>	0.4	<b>0.3</b>	-3.4	<b>-2.7</b>	1.3	<b>0.9</b>	0.5	<b>0.4</b>	0.5	<b>0.1</b>	0.8	<b>0.2</b>	0.5	<b>0.1</b>	1.2	<b>0.9</b>	1.0	<b>0.3</b>	1.9	<b>0.5</b>	1.2	<b>0.2</b>
2	1.5	-1.5	-2.3	0.0	1.9	<b>1.6</b>	-1.0	<b>-1.6</b>	-3.2	<b>-2.1</b>	0.6	<b>-0.2</b>	1.1	<b>0.3</b>	1.3	<b>0.1</b>	2.0	<b>0.2</b>	0.8	<b>0.1</b>	2.3	<b>0.6</b>	3.2	<b>0.2</b>	4.3	<b>0.4</b>	1.6	<b>0.2</b>
3	-0.6	-0.2	-1.4	-1.3	0.4	<b>-0.8</b>	0.6	<b>0.2</b>	-0.7	<b>-1.2</b>	0.1	<b>-1.3</b>	0.1	<b>0.1</b>	0.8	<b>0.2</b>	1.4	<b>0.0</b>	2.6	<b>0.1</b>	0.2	<b>0.1</b>	1.8	<b>0.3</b>	3.1	<b>0.1</b>	5.9	<b>0.2</b>
4	-1.5	-0.4	0.7	-0.4	-1.1	<b>-1.3</b>	-0.1	<b>-0.4</b>	0.6	<b>0.7</b>	0.0	<b>-0.1</b>	0.9	<b>0.1</b>	0.4	<b>0.2</b>	0.8	<b>0.1</b>	0.9	<b>0.1</b>	2.0	<b>0.1</b>	0.9	<b>0.5</b>	1.9	<b>0.2</b>	2.0	<b>0.3</b>
5	1.3	1.0	-1.9	-2.0	0.7	<b>0.9</b>	0.6	<b>0.4</b>	-0.8	<b>-1.7</b>	-1.4	<b>-2.0</b>	1.0	<b>0.2</b>	0.8	<b>0.1</b>	0.9	<b>0.1</b>	1.2	<b>0.2</b>	2.3	<b>0.5</b>	1.6	<b>0.3</b>	2.0	<b>0.2</b>	3.0	<b>0.5</b>
6	-2.4	-1.6	1.2	1.2	-0.9	<b>-1.9</b>	-1.1	<b>-1.8</b>	0.3	<b>0.8</b>	0.7	<b>1.2</b>	0.5	<b>0.2</b>	1.0	<b>0.1</b>	1.2	<b>0.2</b>	0.7	<b>0.1</b>	1.2	<b>0.3</b>	2.2	<b>0.2</b>	2.6	<b>0.5</b>	1.7	<b>0.2</b>
7	1.2	1.0	-4.6	1.2	1.5	<b>1.2</b>	0.9	<b>0.9</b>	-5.6	<b>-4.8</b>	2.0	<b>1.3</b>	0.9	<b>0.7</b>	1.0	<b>0.1</b>	1.6	<b>0.1</b>	0.6	<b>0.2</b>	1.8	<b>1.4</b>	2.2	<b>0.3</b>	3.3	<b>0.2</b>	1.3	<b>0.6</b>
8	1.4	0.0	-1.9	-0.4	1.4	<b>1.3</b>	-1.0	<b>-0.2</b>	-2.3	<b>-2.3</b>	0.1	<b>-0.7</b>	1.3	<b>0.3</b>	0.9	<b>0.1</b>	2.5	<b>0.2</b>	1.7	<b>0.1</b>	3.0	<b>0.6</b>	2.1	<b>0.3</b>	5.7	<b>0.5</b>	3.7	<b>0.2</b>
9	-0.1	0.4	-0.3	-0.5	0.1	<b>0.3</b>	0.0	<b>0.6</b>	-0.4	<b>0.1</b>	-0.5	<b>-0.4</b>	0.4	<b>0.2</b>	0.4	<b>0.1</b>	0.4	<b>0.3</b>	0.8	<b>0.0</b>	0.8	<b>0.5</b>	0.7	<b>0.2</b>	0.8	<b>0.5</b>	1.9	<b>0.1</b>
10	-0.6	-0.6	-0.2	-0.7	-0.1	<b>-0.6</b>	0.0	<b>-0.7</b>	0.1	<b>-0.4</b>	-0.1	<b>-0.8</b>	0.4	<b>0.1</b>	0.3	<b>0.1</b>	0.3	<b>0.1</b>	0.6	<b>0.1</b>	0.9	<b>0.2</b>	0.6	<b>0.2</b>	0.7	<b>0.3</b>	1.2	<b>0.3</b>
11	2.8	-1.7	-3.2	1.6	2.3	<b>2.6</b>	-0.9	<b>-1.2</b>	-3.7	<b>-3.1</b>	1.6	<b>1.3</b>	0.4	<b>0.6</b>	1.2	<b>0.2</b>	1.5	<b>0.1</b>	0.6	<b>0.1</b>	0.9	<b>1.3</b>	2.5	<b>0.5</b>	3.5	<b>0.3</b>	1.5	<b>0.3</b>

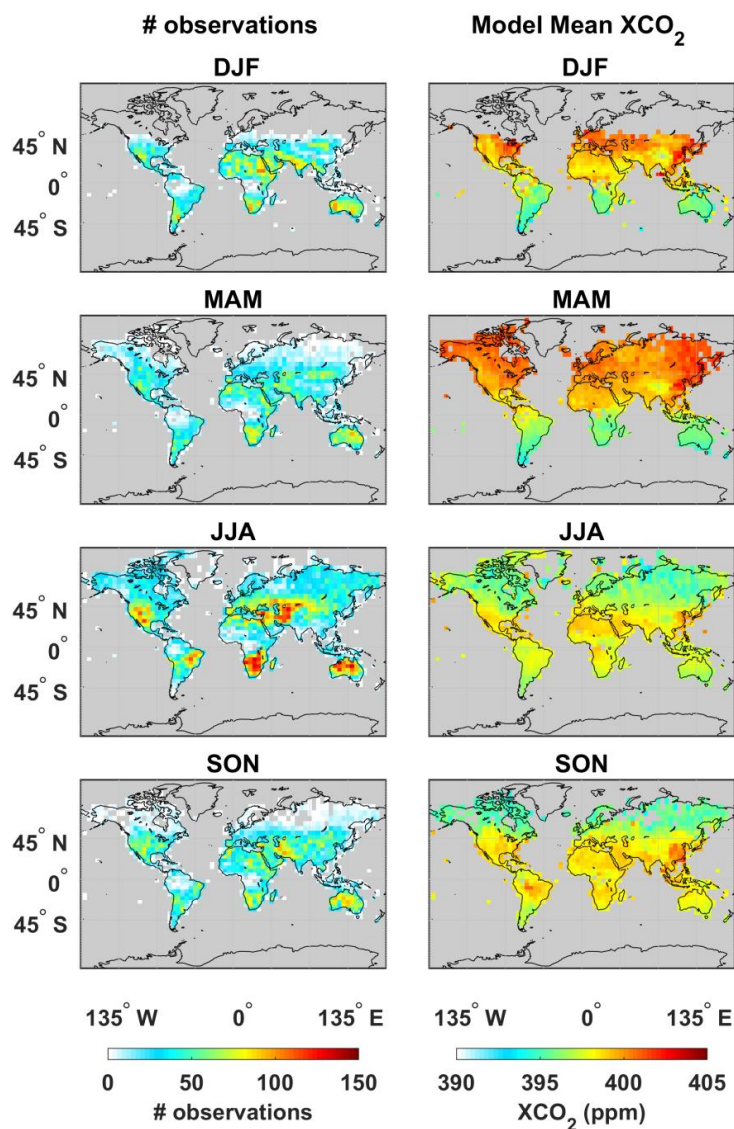
\*TransCom-3 region name and location displayed in Fig. S2.

6  
7



1

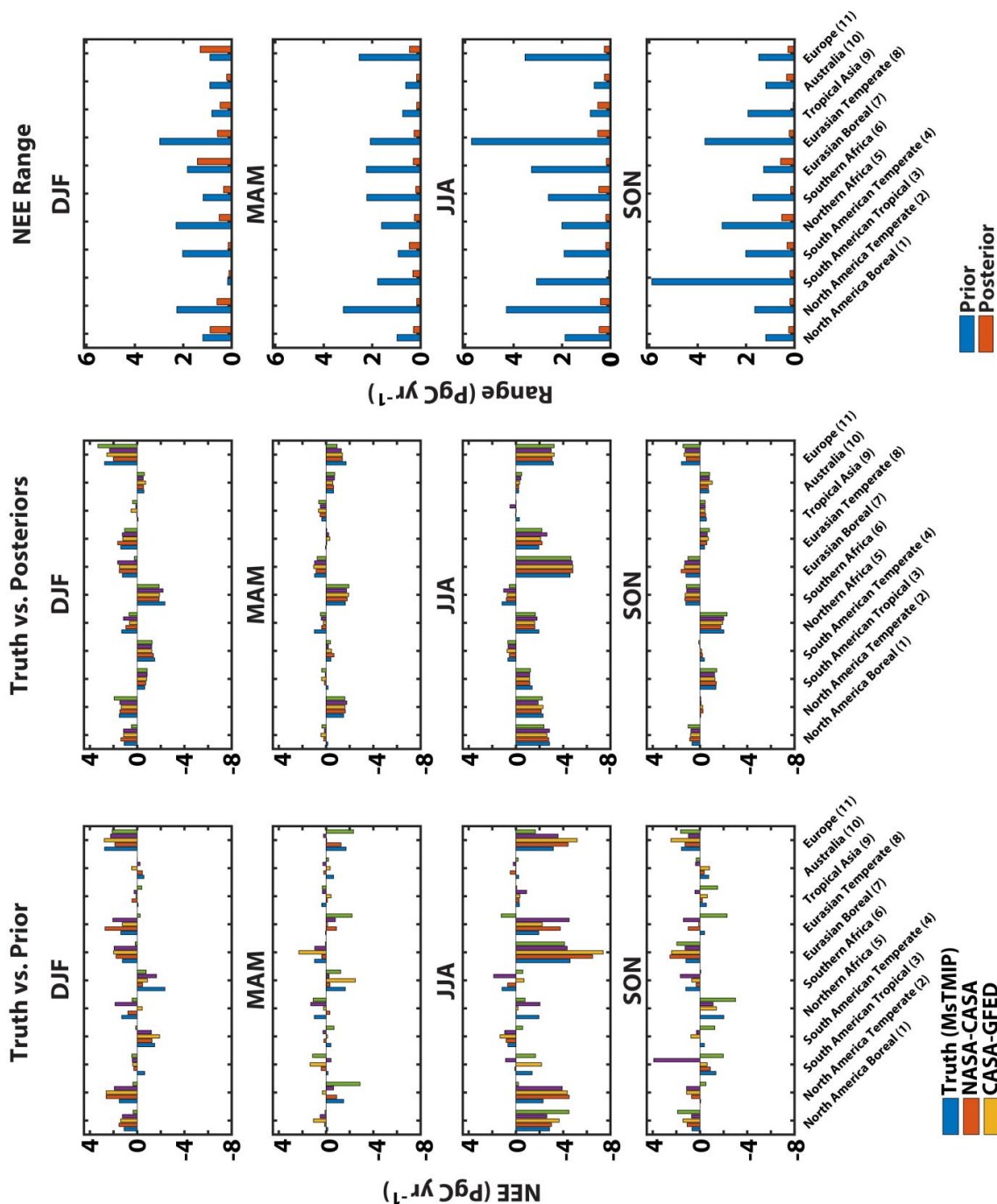
2 **Figure 1: Prior multi-model (NASA-CASA, CASA-GFED, SiB-4 and LPJ biosphere models) seasonally-averaged NEE (gC m<sup>-2</sup> day<sup>-1</sup>)**  
 3 **(left column) and NEE standard deviation (gC m<sup>-2</sup> day<sup>-1</sup>) (right column) for the year 2015.**



1

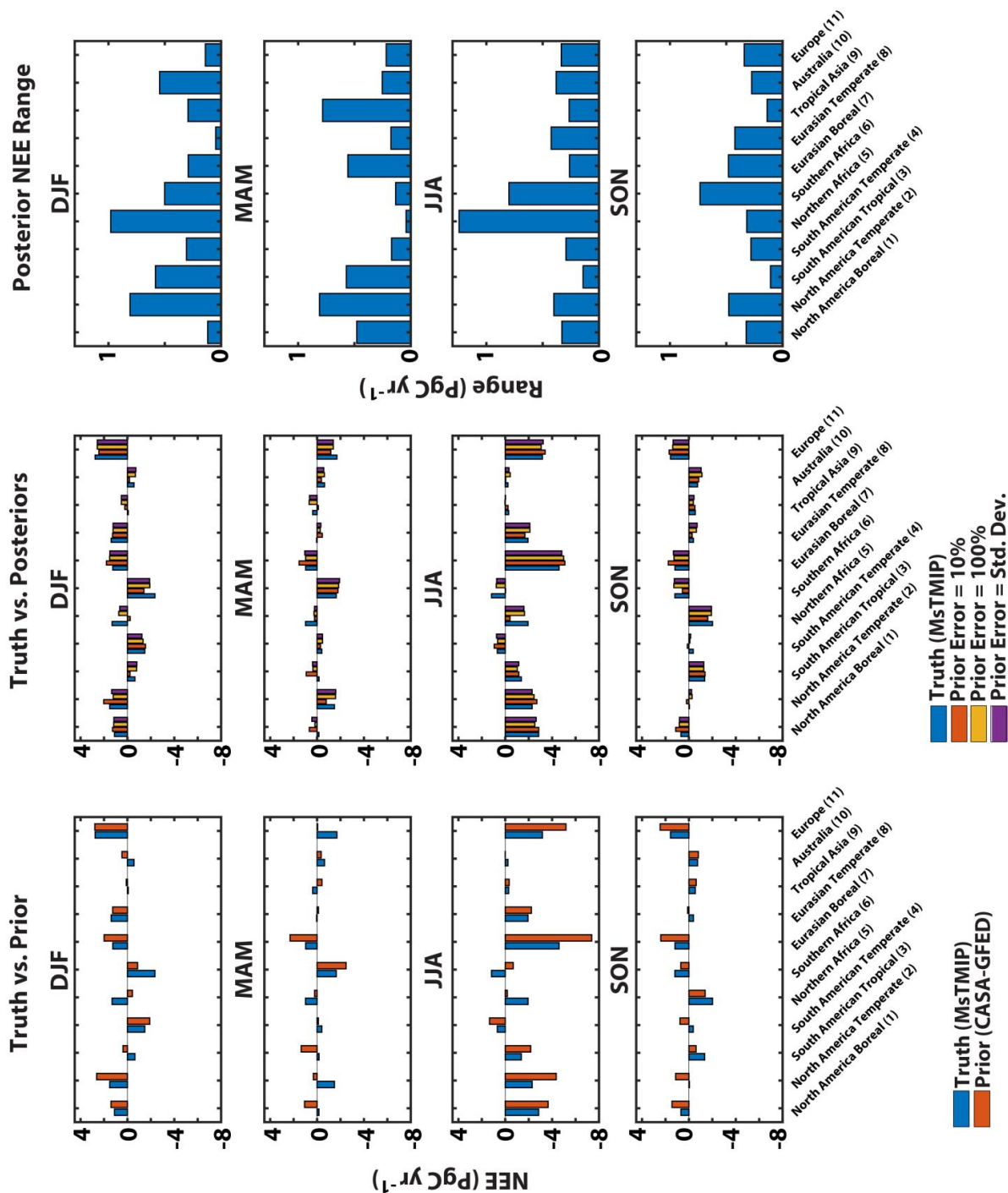
2 **Figure 2:** Total number of OCO-2 LN and LG XCO<sub>2</sub> observations (left column) and the corresponding seasonally-averaged multi-model  
3 (NASA-CASA, CASA-GFED, SiB-4 and LPJ biosphere models) mean GEOS-Chem-simulated prior XCO<sub>2</sub> (ppm) (right column) in 2015.

4



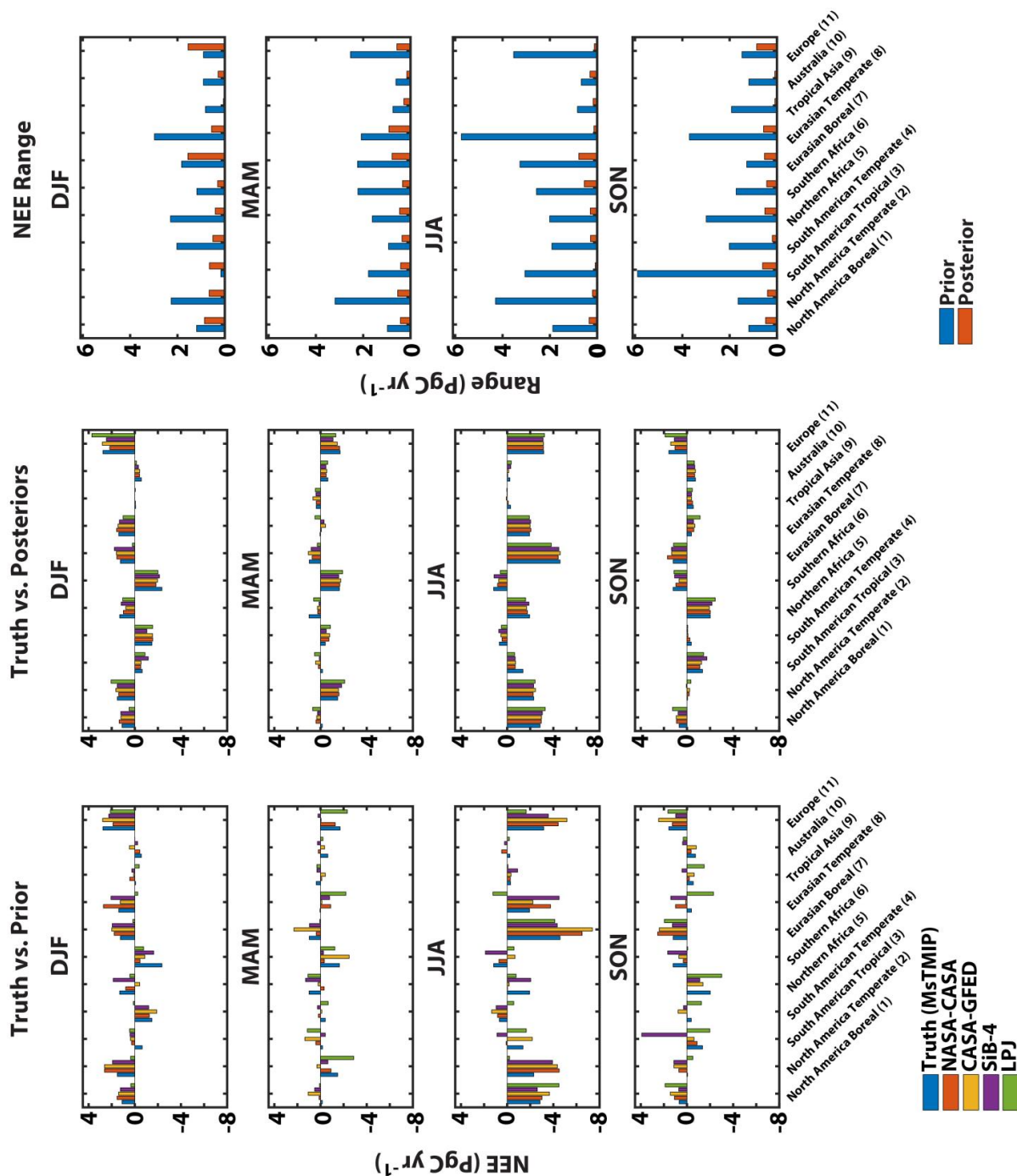
1  
 2  
 3  
 4  
 5  
 6

Figure 3: Seasonally-averaged NEE (PgC yr<sup>-1</sup>) averaged over the 11 TransCom-3 land regions from MsTMIP (“truth”) versus the prior biosphere models (NASA-CASA, CASA-GFED, SiB-4 and LPJ) (left column), posterior estimates (middle column) from the OSSE simulations and the corresponding range of prior and posterior NEE estimates (right column). The synthetic observations in these OSSE simulations correspond to the OCO-2 LN+LG observing modes.



1  
 2  
 3  
 4  
 5  
 6

Figure 4: Seasonally-averaged NEE (PgC yr<sup>-1</sup>) averaged over the 11 TransCom-3 land regions from MsTMIP (“truth”) versus CASA-GFED prior biosphere model (left column), posterior estimates with the three different prior uncertainties (middle column) and the corresponding range of posterior NEE (right column). The synthetic observations in OSSE simulations correspond to the OCO-2 LN+LG observing modes.



1  
2  
3  
4  
5  
6

Figure 5: Seasonally-averaged NEE ( $\text{PgC yr}^{-1}$ ) averaged over the 11 TransCom-3 land regions from MsTMIP (“truth”) versus the prior biosphere models (NASA-CASA, CASA-GFED, SiB-4 and LPJ) (left column), posterior estimates (middle column) from the OSSE simulations and the corresponding range of prior and posterior NEE (right column). The synthetic observations in these OSSE simulations correspond to the OCO-2 OG observing mode.